Spring 2022

Comparative Analysis of Winglet Efficiency on Supercritical Versus Traditionally Cambered Airfoils

Evan Cathers

Recommended Citation

Cathers, Evan, "Comparative Analysis of Winglet Efficiency on Supercritical Versus Traditionally Cambered Airfoils" (2022). *Electronic Theses and Dissertations*. 2410.
https://digitalcommons.georgiasouthern.edu/etd/2410

COMPARATIVE ANALYSIS OF WINGLET EFFICIENCY ON SUPERCRITICAL VERSUS TRADITIONALLY CAMBERED AIRFOILS

by

EVAN CATHERS

(Under the Direction of Mosfequr Rahman)

ABSTRACT

This study serves to define the performance of several industry-recognized and exploratory wing tip devices on aircraft wings utilizing contemporary supercritical airfoil geometry. For comparison, the same examination is performed on a wing comprised of traditionally cambered airfoils, the platform upon which winglets were initially developed. The supercritical wing design is based on that of the Airbus A320, while the conventional airfoil is based upon the Boeing 737-800 platform. Tip devices selected for analysis include blended, raked, split scimitar, fence, and spiroid winglets, as well as tip sails, characterized by the spreading of a bird's primary flight feathers. Methodology for this study includes the k-ε CFD simulation of full-scale wings, from the root profile to the wing tip (not including the fuselage) as well as experimental wind-tunnel testing to substantiate identified trends. Solution metrics include lift and drag forces, their respective coefficients, as well as simulative flow visualization as generated by ANSYS CFD-Post. It is apparent through this work that there exists a distinct difference between the performances of similar winglets on dissimilar airfoils. The supercritical wing proved to perform most efficiently when paired with a spiroid winglet, providing gains of approximately 21% at cruise conditions, while the conventional wing suffered losses with this application. Conversely, the wing composed of traditionally cambered airfoils generated the highest ratio of lift to drag coefficients when utilizing the split scimitar winglet, which happened to be the most detrimental winglet on the supercritical platform. It is the hope of the author that the findings in this study will support further developments in winglet design and application, specifically on the lesser explored spiroid and tip sail geometries.

INDEX WORDS: Winglet efficiency, Lift coefficient, Drag coefficient, Supercritical wing, Camber, Flow visualization, Vorticity, Turbulence, Tip sails, Spiroid, Airbus, Boeing

COMPARATIVE ANALYSIS OF WINGLET EFFICIENCY ON SUPERCRITICAL VERSUS TRADITIONALLY CAMBERED AIRFOILS

by

EVAN CATHERS

B.S., Tennessee Technological University, 2020

M.S., Georgia Southern University, 2022

A Thesis Submitted to the Graduate Faculty of Georgia Southern University

in Partial Fulfillment of the Requirements for the Degree

MASTER OF SCIENCE

ALLEN E. PAULSON COLLEGE OF ENGINEERING AND COMPUTING

COMPARATIVE ANALYSIS OF WINGLET EFFICIENCY ON SUPERCRITICAL VERSUS TRADITIONALLY CAMBERED AIRFOILS

by

EVAN CATHERS

Major Professor:	Mosfequr Rahman
Committee:	Marcel Ilie
	Valentin Soloiu

Electronic Version Approved:
May 2022

DEDICATION

I dedicate this thesis to my parents Amy and Kevin, as well as my Aunt Susan and Uncle Michael. Without their love, patience, kindness, and support, I could never have expected to arrive at this point in my academic career. I hope this thesis serves to begin to show my appreciation and acknowledgement of your sacrifices and motivation to help push me to where I am now.

ACKNOWLEDGMENTS

I would like to recognize Professors Mosfequr Rahman, Marcel Ilie, and Valentin Soloiu of Georgia Southern University for their invaluable knowledge, encouragement, and advice during my research. I extend my gratitude for their willingness to sit on my thesis committee and for taking the time to help guide me through this process. Special thanks also due to Dr Shaowen Xu for his very thorough instruction of modelling and simulation. Without the help of these professors and committee members, the completion of this study could not have been possible.

Furthermore, I would like to acknowledge Professors Ahmad Vaselbehagh and Jie Cui of Tennessee Technological University for thoroughly preparing me for research in fluid mechanics and computational fluid dynamics. Their dedication to their students and career formed a solid foundation from which to build my graduate career.

Lastly, I would like to thank my friends Matthew, Harrison, and Eli for their comic relief during my graduate career, as my stress would have grown uncontrolled. Our game nights served to be very therapeutic.

TABLE OF CONTENTS

Page

CHAPTER

APPENDICES

LIST OF TABLES

Page

LIST OF FIGURES

LIST OF ABBREVIATIONS

A	Planform Area (m^2)
ADC	Analog to Digital Converter
AoA	Angle of Attack (°)
API	Aviation Partners, Inc
AR	Aspect Ratio
C_d	Drag Coefficient
C_l	Lift Coefficient
CoP	Center of Pressure
$C_{1\text{-}3\varepsilon}$	Established K-Epsilon Model Closure Constants
C_μ	Model Coefficient (Eddy Viscosity)
D	Drag Force (N)
DAQ	Data Acquisition (Device)
F	Force (N)
FDM	Fused Deposition Modeling
FR	Froude Number
g	Gravitational Acceleration (m/s^2)
G_b	Kinetic Energy Due to Buoyancy (N)
G_k	Turbulent Kinetic Energy Generated by Velocity Gradients (J/Kg)
k	Turbulent Kinetic Energy (J/Kg)
L	Lift Force (N)
MAC	Mean Aerodynamic Chord (m)
NACA	National Advisory Committee for Aeronautics
NASA	National Aeronautics and Space Administration

P	Pressure (Pa)
PETG	Polyethylene Terephthalate Glycol
q	Dynamic Pressure (Pa)
Re	Reynolds Number
rc	Wing Root Chord
S	Modulus of the Mean Rate-of-Strain Tensor
t	Time (sec)
tc	Wing Tip Chord (m)
TR	Taper Ratio
v, V	Velocity (m/s)
VFD	Variable Frequency Drive
W	Wingspan (m)
Y_M	Contribution of Fluctuating Dilation in Compressible Turbulence to Dissipation Rate
ε	Turbulent Energy Dissipation Rate (W/Kg)
μ	Dynamic Viscosity (Kg/m s)
μ_t	Eddy Viscosity (m^2/s)
ρ	Density (Kg/m^3)
σ_k	Established K-Epsilon Model Closure Constant
σ_ε	Established K-Epsilon Model Closure Constant

CHAPTER 1

INTRODUCTION

1.1 History of Aerodynamic Efficiency Improvements

In the global aerospace industry, manufacturers and partnering agencies are constantly working to design aircraft to operate more efficiently, managing savings both economically and environmentally. Several approaches can be made to accomplish this, including (but not limited to) improving propulsion technology, the fuel it burns to produce thrust, and the physical size, shape, and material of the aircraft's features such as the fuselage, empennage (tail section), and wings. It is also known that the inclusion of wing-tip devices on large passenger aircraft can help improve fuel economy and subsequent cruising range, which saves airline companies millions of dollars a year. In a press release by Aviation Partners, Inc. (API) in 2019 it was projected that by year-end, approximately 10 billion gallons of jet fuel had been saved since their introduction of blended and split-scimitar winglets in 1999 in partnership with Boeing (Aviation Partners, Inc. 2019). Shown below in Figure 1 is Boeing's implementation of this blended winglet on its 737 series passenger aircraft.

Figure 1. API Blended Winglet Technology for Boeing 737 Model (Boeing 2022)

In recent decades, designs for most large passenger jet wings have been based on supercritical airfoils, which have a slightly different profile than the previous conventional airfoils. This more aggressive airfoil features a flattened upper surface and concave curvature to the underside of the airfoil's trailing edge, whereas the traditional airfoils before this consisted of convex curvature on top, and a flattened underside. Dr Richard Whitcomb, a renowned aeronautical engineer, developed this change in wing cross section in 1969. This individual is also responsible for developing wing-tip devices. The flat surface along the top of the airfoil results in a slower propagating shock wave on the wing's upper surface, delaying the onset of boundary layer separation and resulting drag production at the cost of reduced lift. To counter this loss, the signature downward curve of the supercritical airfoil's trailing edge was included to produce more lift (The National Aeronautics and Space Administration 2008).

However, this airfoil design does not compensate for lift-induced drag. This phenomenon is produced by the difference in pressure gradients on the upper and lower surfaces of a wing. The pressure generated underneath the wing is higher than that above the wing, and thus tends to travel around the end of the wing, circulating clockwise around a plane's left wing and counterclockwise around its right wing (when viewing the aircraft from the rear). This rotation causes vorticity, which can interfere with the lift producing capabilities of the plane's wings. To counter this, wing-tip devices have been developed and implemented on several types of aircraft around the world, proving to offer fuel consumption reductions in the range of 2.2% to 6% depending on plane model and configuration, as reported by major airlines. These wing-tip devices accomplish this task by changing the way that pressure fields interact with the structure of the aircraft's wings during flight. These winglets extend the span of each wing, causing the movement of the pressurized pockets under the wings to travel further away from the lift-producing profiles of the wing before rotating upwards and joining the low-pressure region above the wing. As a result, the vorticity produced is moved further outwards, enabling the airfoil's design to produce lift more efficiently.

1.2 Evaluation Methods

In the past, evaluation of aircraft wing modifications had been based on observation and the application of general aerospace principles, as modelling flows and resulting forces with detail was not possible. Equipment such as wind tunnels were and continue to be used to determine the most efficient airfoil shapes, beyond what mathematicians could model from principles based in fluid dynamics. This method led to today's flow visualization techniques, which involve introducing a very fine particulate such as hydrogen bubbles, dye, or smoke to the flow of a wind tunnel. This particulate then flows over the wing mounted inside the tunnel to provide a visual approximation of how the air flow interacts with its surfaces, showing where boundary layer separation and vortex production occur. Alongside this, force balances can be constructed with load cells to determine the forces exerted on an object in the tunnel, such as lift and drag.

Computational fluid dynamics has proven to be an invaluable resource in the modern era for its uses in assessing the performance of several aerospace applications due to its ability to determine several parameters with high accuracy while incurring no material cost. Numerous boundary conditions and models such as the shear stress transport k-omega (SST k-omega) or k-epsilon model can be applied to analyze certain aspects of a wing by subjecting it to varying types of flows and conditions. Post processing can be utilized to show exactly where stresses, pressures, temperatures, or other metrics occur and at what magnitude. The center of pressure (CP) of the wing can also be easily determined, which is the location in three-dimensional space where the total sum of all pressure fields and resultant vectors, namely lift and drag, act upon. Using this location, the mounting point for the wing can be determined when positioning it inside the wind tunnel, allowing for accurate force balance measurement. When combined, these techniques serve to provide a robust assessment of wing and winglet capabilities without requiring costly experimental prototypes or full-scale flight testing.

1.3 Study Contribution

The goal of this research was to determine the capabilities of winglets as they are applied to a more aggressive, contemporary wing design, such one incorporating supercritical airfoil profiles and substantial twist. A parallel comparison to traditionally cambered wings was also completed to determine a basis from which to substantiate unique results. Numerous studies similar in methodology to this have already been performed on wings with more traditional airfoils. The aerospace field has since expanded with new wing advancements by several manufacturers around the world. The selected wing-tip devices represent a broad range of designs in the aerospace industry, including some that have been developed and used for numerous years, and some that have yet to be explored further. The outcome of such experimentation provides a broadened indication of the performance of modern wing-tip devices. To investigate this topic, the author has conducted computational fluid dynamics simulations which were intended to identify which winglets provide the highest aerodynamic efficiency under ascending, cruise, and descending operating conditions. These theoretical results were then validated by force balance measurement and flow visualization techniques of scale models.

1.4 Experimental Hypothesis

Wings composed of supercritical airfoils provide higher aerodynamic efficiency over traditionally cambered airfoils due to heightened flow velocity above the wing’s upper surface, reducing the magnitude of the shockwave and relocating it as far aft as possible causing layer separation and the resulting drag to be minimized. If several established and exploratory wing-tip devices are applied to wings of both airfoil types, distinctly varied winglet suitability will be identified regarding airfoil type due to modified spanwise flow and vortex production of each wing. The trends identified in this study should distinguish which winglet technologies have potential for further investigation in modern aircraft efficiency studies.

CHAPTER 2

LITERATURE REVIEW

2.1 Airfoil Characterization

2.1.1 Traditionally Cambered Airfoil Designs

Modern airfoils are defined by several geometric parameters, which aid in characterizing them for certain applications. The National Advisory Committee for Aeronautics (NACA), now known as the National Aeronautics and Space Administration (NASA), maintains a large database of airfoils classified by multiple categories which utilize a name/numbering convention by which to easily identify airfoil parameters. These specific identifiers typically include information regarding pressure distributions at specific locations along the profile, chord length, expected lift coefficient, camber percentage, and the location of maximum thickness. In the figure below, the geometric parameters of a NACA 2412 4-digit airfoil (maximum camber of 2% located at 40% chord, with maximum thickness of 12% of the chord).

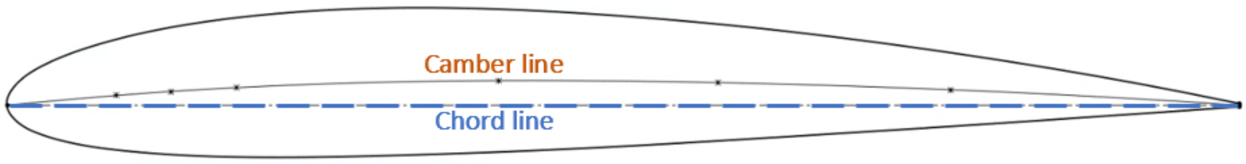

Figure 2. NACA 2412 Cambered Airfoil Profile

As can be seen by Figure 2 above, this airfoil is asymmetric as shown by the camber line. Symmetric and asymmetric airfoils differ only by this parameter, as symmetric airfoils simply have no camber. Symmetric airfoils have been found to aid in applications where significant maneuverability is required, such as rolling. For this reason, the airfoil must be able to produce lift in many different orientations. By this principle, they also make for an excellent choice for components such as rudders and elevators. However, symmetrical airfoils also produce significantly more drag than those with camber, and thus produce lift with less efficiency. In fact, at a 0° angle of attack, they produce no lift whatsoever. It is for this reason that this type of airfoil is used sparingly on aircraft, typically only being implemented as main wings on planes used for aerobatics. Cambered, or asymmetric airfoils are designed in such a way that optimizes the production of lift at the cost of some maneuverability.

Lift generation as it is understood today can be described by two main principles dating back as far as 336 years ago as theorized by English mathematician Isaac Newton and Swiss mathematician Daniel Bernoulli. Newton’s third law states that for every action, there is an equal and opposite reaction. In terms of airfoils, any portions of the flow that are redirected downward by the airfoil have an equal and opposite force in the upwards direction (relative to the airfoil) which constitutes lift force. That is why the AoA has such a significant effect on the functionality of lift generation, especially for symmetric airfoils. Bernoulli’s principle is based on the relationship between pressure and velocity and is shown in Eq. (1).

$$P + \frac{1}{2}\rho\, V^2 = constant \tag{1}$$

where P is pressure, ρ is fluid density, and V is flow velocity. In this relationship, if pressure increases, velocity decreases. Likewise, if velocity of the flow increases, the pressure becomes lower. When a flow is introduced to a symmetrical airfoil, the velocity around the airfoil is the same on both top and bottom resulting in equal amounts of pressure, again making angle of attack paramount to generating lift. However, with an asymmetric airfoil, the cambered geometry interacts with the flow to create a difference in velocities along the top and bottom surfaces. The upper portion’s higher curvature allows for a greater velocity flow while the opposite can be said about the flow underneath the foil. This creates a low-pressure region above the airfoil and high-pressure underneath, causing lift generation to occur as shown in Figure 3. Because of this principle, some asymmetrical airfoils can produce lift with even a slightly negative angle of attack, such as the 65_2-415 NACA airfoil. Its zero-lift AoA is found to be at -2.6° (Gudmundsson 2014).

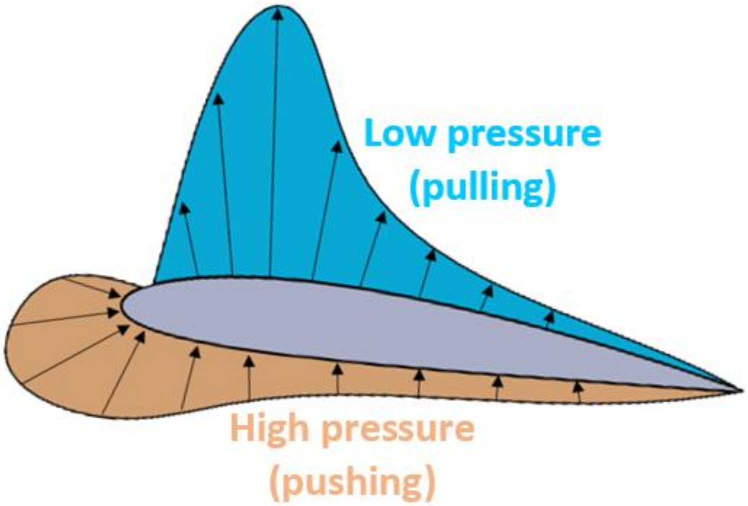

Figure 3. Localized Airfoil Pressure Region

2.1.2 Supercritical Airfoil Designs

Supercritical airfoils, as determined by Whitcomb, further harness these principles to create a foil which provides even more efficient operation. Similar in function to its traditionally cambered counterpart, its camber and geometry result in significant differences in pressure gradients. However, this type of profile features a more flattened upper surface, while the underside has convex curvature from the leading edge to approximately 75% of its chord length, and then curves downwards at the trailing edge forming slight concavity. This allows for slightly more exaggerated benefits as those observed of the traditionally cambered airfoil. Additionally, because of this exaggerated effect, the shock wave caused by the increased flow velocity is formed near the trailing edge of the profile, resulting in far less boundary layer separation than the other airfoils mentioned. Figure 4 shows this occurrence. This boundary layer separation is what results in the production of turbulence behind the entire span of a plane wing, which can interfere with the structure’s lift producing abilities. The aggressive curvature at the rear of the foil is also responsible for additional drag production known as form drag (Winslow, et al. 2018). However, this slight increase in drag does not outweigh the benefits of increased lift generation.

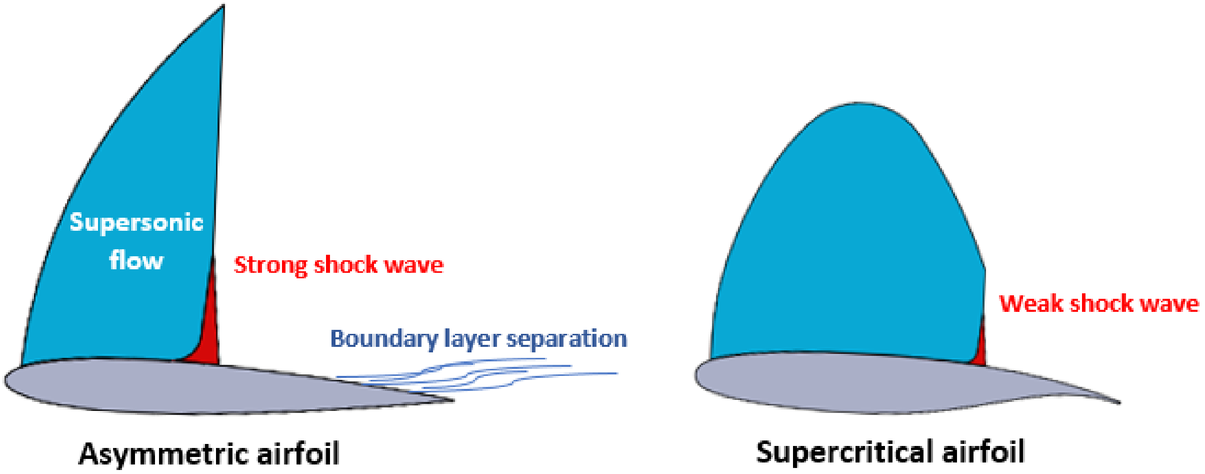

Figure 4. Flow Characteristics of Traditional and Supercritical Airfoils

Due to the development of knowledge surrounding airfoil technology and fierce market competition, most aircraft manufacturers have developed and maintained proprietary airfoil designs to sustain a competitive advantage. However, older designs have been released and inferences can be made based on visual inspection and the existence of similar NACA profiles.

2.2 Wing Shape Development

Aircraft wings are manufactured in several different shapes and sizes based on the cargo a plane is intended to carry, the distance it needs to travel, and desired handling / performance capabilities. Because of this, there are numerous industry-standard parameters that must be considered when designing plane wings. The wingspan of an aircraft is the distance from one wingtip to the other. Following this is the aspect ratio AR, utilizing the expression below in Eq. (2) to define the ratio of a wing's span W to its planform area A (NASA John H. Glenn Research Center 2021).

$$AR = \frac{W^2}{A} \tag{2}$$

As the previous expression shows, wings with large spans will typically be slender in form, of course depending on planform area. Longer, more slender wings tend to be more stable and efficient while producing less lift-induced drag as a wing with lower aspect ratios. Conversely, wings with lower aspect ratios such as those on fighter jets have higher agility. In industry, it is typical for subsonic aircraft to have an *AR* in the range of 6 to 10 (Kermode, Barnard and Philpott 2006).

2.2.1 Spanwise Geometry Definition

Except for straight leading and trailing edge aircraft, wings incorporate several different airfoils at their roots, midspan sections, and tips. By doing so, a wing's aerodynamic properties can be optimized at all locations across its span. For example, at the root of a wing, the forces are the greatest such as a loaded cantilever beam. This is where the integrity of the wing must be the strongest, so it must use a thicker, broad-nosed airfoil profile. This area of the wing must also be where the stall-condition, or loss of lift due to low air speed must occur. This occurs when the angle of attack is too great for the current speed of the aircraft (Shih, et al. 1992). If the tip of the wing is the last to stall, the plane can maintain moderate levels of control until all lift generation has diminished. The midspan airfoil is where the typical kink is observed in most large, swept-wing passenger aircraft. This is where the lofted shape of the wing transitions from the thicker root profile to the much thinner, shorter tip airfoil. When all selected airfoils are incorporated with the planform, or the two-dimensional layout of the wing and fuselage structure, the general shape of the wing can be defined (Güzelbey, Eraslan and Doğru 2018).

The planform does not, however, specifically define sweepback and dihedral angles or degrees of twist at each airfoil location. The utilization of a swept wing in modern-day aircraft is due to discoveries made by Robert T. Jones, a renowned aerodynamicist of the 20th century. He was awarded the Langley Medal of the Smithsonian Institution, a prestigious recognition bestowed on the Wright Brothers, Charles Lindbergh, Robert Byrd, and James Webb (National Aeronautics and Space Administration 2017). He theorized that utilizing a swept wing would help improve efficiency by splitting the flow into two components. In terms of aircraft wings, air velocity is split into two components. One component is along the wing's span, while the other is perpendicular to it. The first does not influence the aircraft; the second component normal to the wing contributes to drag. Following this principle, the shock waves caused by the accelerated flow above an airfoil always form perpendicular to it. As shown in Figure 5, if the wing is swept back, this shock wave is split into two components, with only one contributing significantly to drag production (Vincenti 2005).

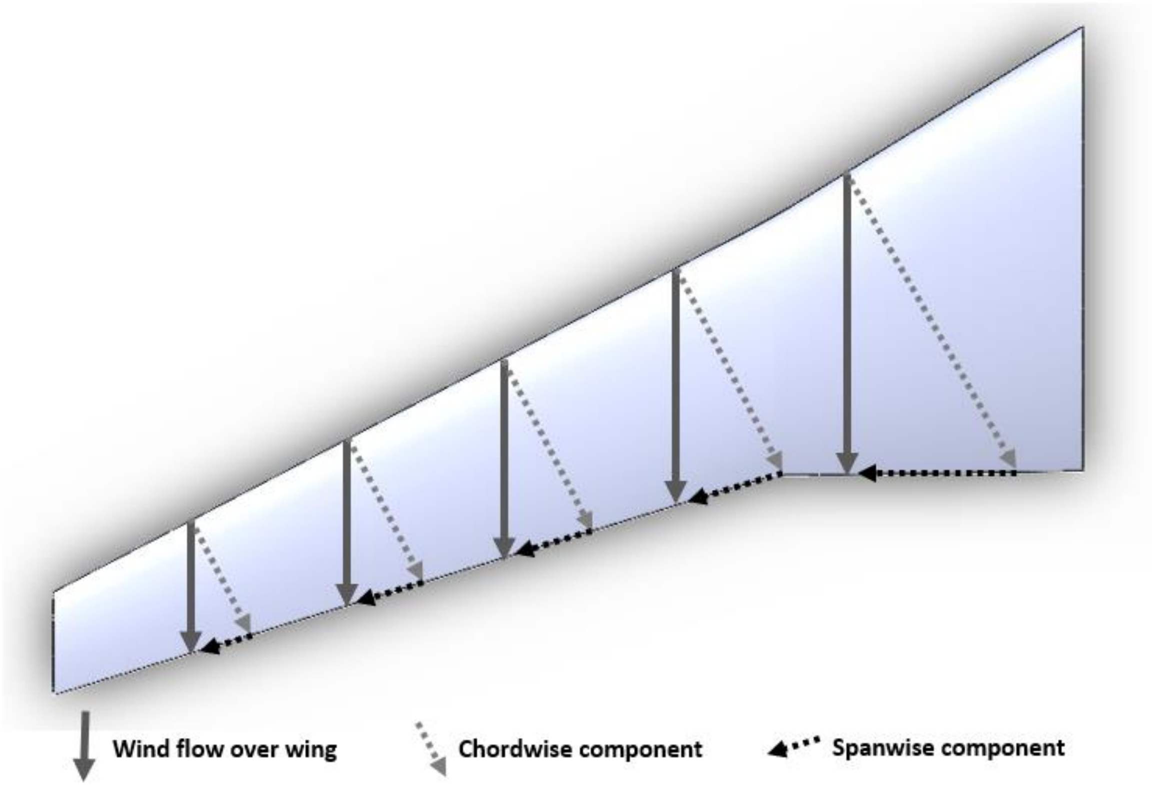

Figure 5. Velocity Components of Swept Aircraft Wings

2.2.2 Wing Dihedral and Twist Angles

The inclination of an aircraft's wings from root to tip is known as the dihedral angle. This is named after the dihedral effect, in which a rolling moment is applied to the aircraft due to its non-zero angle of sideslip. When a plane is in operation, the vector in which it is flying may not be quite the same as the vector at which the airflow or wind is meeting the aircraft (Roskam 1979). By applying this inclination to the wings, the aircraft can maintain rolling stability when experiencing conditions such as crosswinds. Lastly, the degrees of twist applied to the wing at each airfoil helps aid in lift distribution. As mentioned previously, wings are designed in such a way that stall occurs at the root first. By modifying the angle of attack of each individual airfoil, or applying a degree of twist at each location, this condition can be satisfied. Additionally, if a certain airfoil design has a high zero-lift AoA, it must be angled as such to maintain lift production.

2.3 Wing-Tip Devices

Following efforts to improve aircraft efficiency through base wing modification, it was found that wing-tip devices, first discovered by Whitcomb, could provide a reduction in drag production on modern aircraft. The function of a winglet is to help reduce and relocate vortices produced because of lift-induced drag. This drag occurs due to the lift-generating pressure difference above and below a wing. The pressurized flow moves laterally from the underside of the wing, rotates around the tip, and back towards the root above the wing into the lower pressure region where higher velocity flow occurs. This introduces inwards rotation to the wake of the wing, which can interfere with the wing’s ability to produce lift. A winglet’s design elongates the structure and moves the vortex of the turbulence up and away from the main wing, thus improving its efficiency.

Several varieties of wing-tip devices have been designed; some having been in use in the aviation industry for years. In an interview conducted with Joe Clark, the president of API in 1999, it was stated that flight tests conducted using blended winglets on the Boeing 737-400 resulted in a 7% drag reduction. However, it was also mentioned that wind tunnel testing using physical prototypes only indicated a 2% drag reduction, so caution was aired when viewing scaled experimental results (Clark 1999). Others are more aggressive and of more contemporary design and have not yet been implemented in mass configurations due to a lack of research validation and industry demand. One such example is found in a study based on biomimicry of birds. It was theorized that the split wingtips, or space between flight feathers, was an evolutionary trait developed to make flight easier by decreasing induced drag. Experimentation had shown that a “feathered tip” provided a 6% decrease in drag on wings with a conventional Clark-Y airfoil (Tucker 1993). In Figure 6, several winglet types known to the aviation industry are shown.

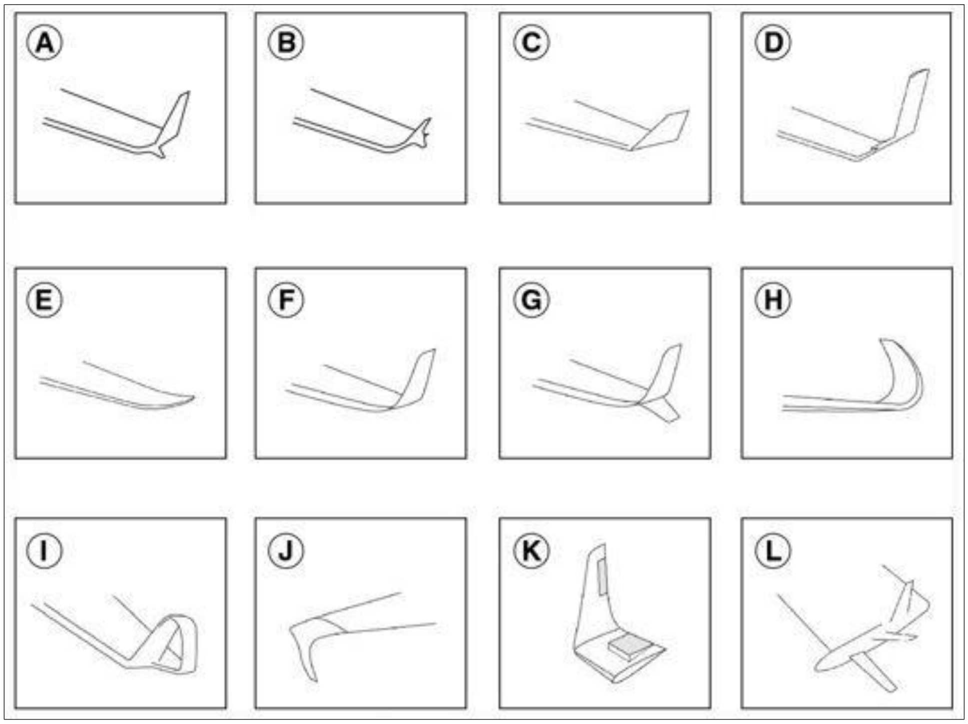

Figure 6. Current Industry Wingtip Devices (Guerrero, Sanguineti and Wittkowski 2020)

(A) Whitcomb winglet. (B) Fence winglet. (C) Canted winglet. (D) Vortex Diffuser. (E) Raked Winglet. (F) Blended winglet. (G) Split scimitar winglet. (H) Sharklet. (I) Spiroid winglet. (J) Downward canted winglet. (K) Active winglets. (L) Tip sails.

CHAPTER 3

METHODOLOGY

3.1 Wing & Winglet Model Selection

For the purposes of this study, a supercritical wing based on the Airbus A320 was chosen for its aggressive, contemporary design characteristics. The Boeing 737-800's wing design was selected to provide a comparison to a fundamental wing platform on which several winglets were implemented in many varieties on a large scale. Airbus was the manufacturer of one of the first large passenger aircraft in the early 1980s to include a supercritical airfoil with its A310-200 model (Petrescu, et al. 2017).

3.1.1 Wing Design Selections

Due to the proprietary designs of Airbus, limited specifications were available in published works, such as sweep angle, approximated chord lengths, and spanwise airfoil profile positions. Other specific design parameters were selected based on aircraft of comparable size and common supercritical profiles as defined by NACA and NASA. Following this, images of Airbus A320 wings were also analyzed to help validate airfoil profile selections, twist, and angles of attack. Only the portions of the wings beyond the fuselage section were modelled, as the lift and drag produced by the cylindrical body of the aircraft is beyond the scope of this study. Shown below in Table 1 are the derived geometrical characteristics for the selected wings.

Table 1. Selected Wing Design Parameters Based on the Airbus A320 and Boeing 737-800

Specification type	Wing Composed of Supercritical Airfoils	Wing Composed of Traditionally Cambered Airfoils
Wingspan (one wing, no winglets)	15 [m]	15 [m]
Sweepback angle (at 25% chord)	25.°	25°
Dihedral angle	5.11°	6.00°
Airfoil selections (Root & midspan 1, midspan 2 & tip)	NASA SC(2)-0714, NASA SC(2)-0414	b737a-il, b737b-il, b737c-il, b737d-il
Spanwise airfoil location (Root, midspan 1, midspan 2, tip)	0, 4.5, 10.5, 15 [m]	0, 3.75, 9.375, 15 [m]
Chord lengths (Root, midspan 1, midspan 2, tip)	6.5, 3.75, 2.46, 1.5 [m]	5.71, 3.38, 2.31, 1.25 [m]
Degree of twist (Root, midspan 1, midspan 2, tip)	+4.5°, 0°, 0°, -2°	0°, 0°, 0°, 0°

To model the wings, solid modeling program SolidWorks by Dassault Systèmes was used. A full-scale left-hand wing was modelled, as the viewing pane of the wind tunnel used in physical investigations is oriented as such. Sketches of the selected airfoils were projected on planes based on span-wise location. These sketches were then translated the proper distances upwards and rearwards to account for sweepback and dihedral angle. Following this, a series of three-dimensional sketches were used to connect each profile at leading and trailing edge, providing guide rails for the loft tool to reference when constructing the model. The base wings as designed in SolidWorks are shown below in Figures 7 and 8.

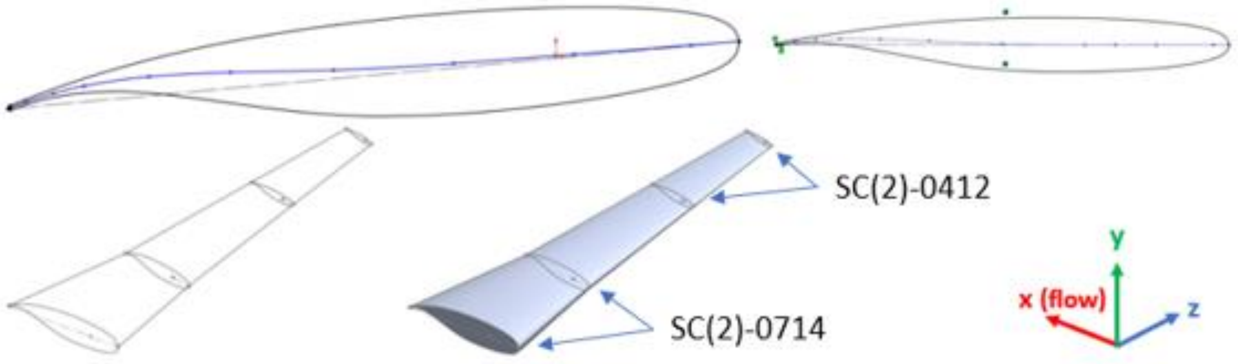

Figure 7. Supercritical Wing Solid Modeling Loft Geometry

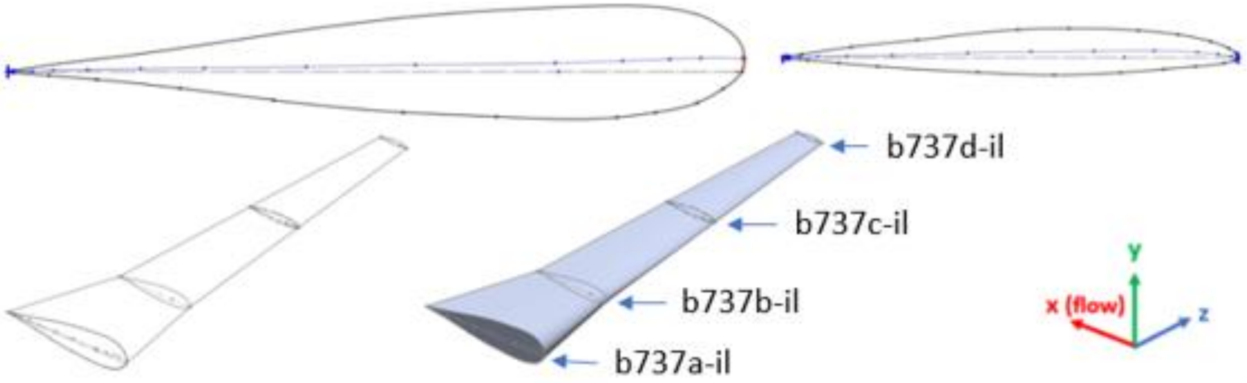

Figure 8. Traditionally Cambered Wing Solid Modeling Loft Geometry

3.1.2 Winglet Design Selections

Following this, winglets of the following types were selected for the study: blended, split scimitar, wing-tip fence, raked, wing-tip sails, and spiroid. The blended and split scimitar winglets were chosen based on their prevalence across the aerospace industry, as well as for their proven efficiency improvements. The wing-tip fence was selected for its origins with Airbus, and the raked for its use on long-range aircraft. Lastly, the wing-tip sails were elected for their contemporary, biomimetic characteristics and the spiroid winglet for its unconventional shape. It is the hope of the author that these selections will broadly represent the current winglet designs researched to date.

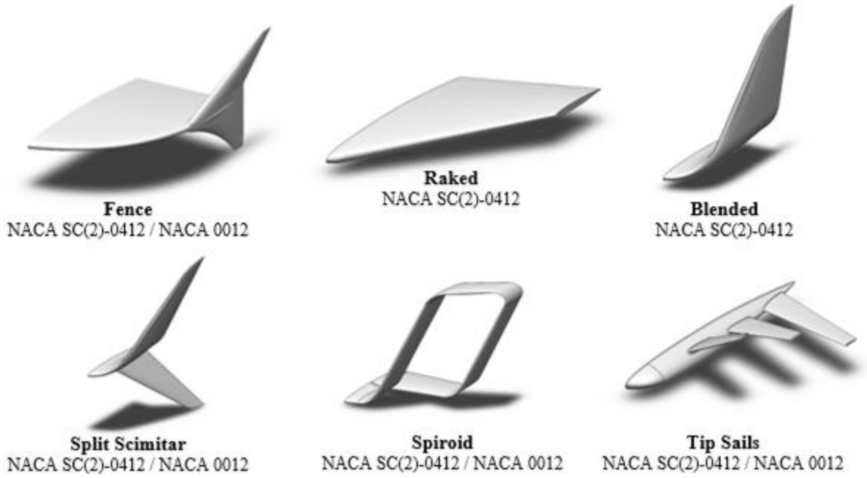

Figure 9. Winglets Selected for Study

Figure 9 above shows the winglets selected and designed for this study. Methods for modelling these wing-tip devices were very similar to that of the base wing, in that several sketch profiles were created and connected with 3D sketch lines (guide curves) to aid in a loft-based build process. Several design criteria for the blended, split scimitar, wing-tip fence, and raked winglets were based on previously configured winglets to give the most accurate representation of the winglets currently used in the aerospace industry. As concluded on a study of efficiency based on winglet cant angle, it was found that out of eight winglet designs, a 60° cant angle proved to be the most efficient (Krishnan, et al. 2020). On a technical site detailing Boeing aircraft technology, heights of the top and bottom fins on the Advanced Technology winglets on the 737 MAX are reported to be 8 foot, 3 inches and 4 feet, 5.8 inches respectively (Brady n.d.). From those height measurements and optimal cant angle, the designs of the blended and split scimitar winglets were designed. The wing-tip fence and raked tips were approximated from the design employed on Airbus and Boeing aircraft. Following this, the wing-tip sails were modeled after a design determined in a paper submitted to the 27th International Congress of the Aeronautical Sciences. A series of three sails were modeled at varying cant angles and tested to determine which setup provided the greatest lift to drag coefficient, which was found to be 12.29, a 7.34% increase over the baseline 11.45 of the bare wing (NACA 23015) (Cosin, et al. 2010). This was accomplished with sails at cant angles of 30, 15, and 0 degrees from leading to trailing edge. Chord positions for each sail were at 30%, 52.5%, and 75% from the leading edge as described by an article in the Journal of Engineering Science and Technology in 2006 (Al-Atabi 2006). Lastly, the spiroid winglet was designed with an additional airfoil as detailed by a study in 2012 on the biomimetic spiroid winglet. As the flow rotates around the end of the wing and winglet, the surfaces of the winglet function as smaller lift-generating surfaces. To counteract downward forces from an upside-down asymmetric foil at the top of the spiroid shape, the NACA 0012 airfoil was chosen for its mild symmetrical characteristics (Guerrero, Maestro and Bottaro 2012). The symmetrical foil was chosen for the top of the spiroid only, with the vertical portions and bottom portion remaining as the NASA SC(2)-0414 profile.

3.2 Computational Fluid Dynamics

3.2.1 Simulation Model

In the simulative portion of this study, solution methods were selected based on their ability to solve for turbulent flows and vorticity formation behind an aircraft wing in flight. To accomplish this, a realizable K-Epsilon model with non-equilibrium wall functions was selected. K-Epsilon models are known for their ability to solve for mean turbulent conditions in high-Reynolds flows both near and remote from wall boundaries (Jones and Launder 1972). The realizable formulation for turbulent viscosity is utilized to more accurately predict the formation of vortices and the rates at which they spread. Non equilibrium wall functions were selected due to the presence of adverse pressure gradients such as those responsible for lift generation inherent to airfoils, as well as to predict flow separation and stagnation (ANSYS 2009). The transport equations for k and epsilon are shown below in Eq. (3) and Eq. (4) respectively.

$$\frac{\delta}{\delta t}(\rho k) + \frac{\delta}{\delta x_j}(\rho k u_j) = \frac{\delta}{\delta x_j}\left[\left(\mu + \frac{\mu_t}{\sigma_k}\right)\frac{\delta k}{\delta x_j}\right] + G_k + G_b + \rho\varepsilon - Y_M + S_k \tag{3}$$

$$\frac{\delta}{\delta t}(\rho\varepsilon) + \frac{\delta}{\delta x_j}(\rho\varepsilon u_j) = \frac{\delta}{\delta x_j}\left[\left(\mu + \frac{\mu_t}{\sigma_\varepsilon}\right)\frac{\delta\varepsilon}{\delta x_j}\right] + \rho C_1 S\varepsilon - \rho C_2\frac{\varepsilon^2}{k + \sqrt{(\nu\varepsilon)}} + C_{1\varepsilon}\frac{\varepsilon}{k}C_{3\varepsilon}G_b + S_\varepsilon \tag{4}$$

These transport equations for k and epsilon require the following coefficients as defined in the relationships shown in Eq. (5), Eq. (6), and Eq. (7).

$$C_1 = max\ [0.43, \frac{\eta}{\eta + 5}] \tag{5}$$

$$\eta = S\frac{k}{\varepsilon} \tag{6}$$

$$S = \sqrt{(2S_{ij}S_{ij})} \tag{7}$$

In Equation 3, G_k represents the turbulent kinetic energy generated by velocity gradients, G_b is the kinetic energy due to buoyancy (not applicable in this study), and Y_M is the contribution of fluctuating dilatation in compressible turbulence to overall dissipation rate. $C_{1\varepsilon}$ = 1.44, C_2 = 1.92, σ_k = 1.0, and σ_ε = 1.2 are established model constants. The difference between the realizable and standard k-epsilon models is the model coefficient for the eddy viscosity as shown in Eq. (8).

$$\mu_t = C_\mu \frac{k^2}{\varepsilon} \tag{8}$$

In this expression, C_μ is the model coefficient, k is the turbulent kinetic energy, and ε is the turbulent energy dissipation rate. This model coefficient is made a variable in the realizable system of transport equations to help predict complex secondary flow features after flow separation (OpenFOAM 2016).

3.2.2 Simulation Boundary Conditions

The simulation boundary conditions such as inlet velocity and direction as well as physical flow parameters such as density and viscosity were held constant, only altering the direction of the flow for all cases to easily modify angle of attack without reconstructing the domain for each simulation execution. These angles of attack, or the vector at which the flow enters the inlet of the simulation's inlet, were set to 0°, 2°, 4°, 6°, and 8° for the wing composed of supercritical airfoils, and 2.5°, 4°, 6°, and 8° for the wing composed of traditionally cambered airfoils to represent the aircraft under various conditions such as climb and steady cruise. The wing designed with supercritical airfoils is at cruise when the aircraft's AoA is 2°, and the wing designed with traditionally cambered airfoils is at cruise when it is at an angle of 6°. The AoA magnitudes for the second airfoil were modified to match relative lift production of the first airfoil due to its lack of twist angle in its design. This characteristic caused lift production from 0° to 2° AoAs to be exceptionally low. Following this, no crosswinds were included in the scope of this study. Velocity was maintained at 230 m/s, as this is the mean cruising speed for aircraft with the same relative magnitude, wingspan, passenger capacity, and travel range as investigated in this study (such as the Airbus A320/A321 model range, as well as the Boeing 737-800 series passenger jet). This corresponds to a Mach number of approximately 0.78, which is just short of the transonic range. The density and dynamic viscosity of the fluid are defined as 0.3414 kg/m^3 and 1.428e-5 kg/m-s to represent the boundary conditions present at a cruise altitude of 11.5 km, representative of aircraft utilizing this wing geometry. The approximate temperature at this altitude is set at 217.79 K. These parameters were utilized to calculate the Reynolds numbers for both wings (with no winglet applied) at their respective mean aerodynamic chord (MAC). Equation (9) and (10) show the expressions utilized to determine the MAC of a swept wing.

$$MAC = \frac{2rc}{3}\,\frac{(1 + TR + TR^2)}{(1 + TR)} \tag{9}$$

$$TR = \frac{tc}{rc} \tag{10}$$

In these expressions, *tc* is the length of the tip chord, *rc* is the length of the root chord, and *TR* is the ratio of the tip chord to the root chord (taper ratio). The supercritical wing's root and tip chords of 6.5 and 1.5 meters resulted in a MAC of 4.521 meters. The conventional airfoil's root and tip chords of 5.71 and 1.25 meters resulted in a MAC of 3.957. These mean chord lengths were then used to estimate the Reynolds numbers using the expression in Eq. (11).

$$Re = \frac{(\rho v MAC)}{\mu} \tag{11}$$

In this expression, ρ is the fluid density, v is the flow velocity, and μ is the dynamic viscosity. As a result, the supercritical wing was subjected to a flow with a Reynolds of approximately 24.9x10^6 and the conventional to a flow with a Reynolds number of 21.8×10^6. These Reynolds numbers are comparable to the expected flows experienced by several models of airliners in industry today when operated at or near maximum cruising altitude (Sforza 2014).

3.2.3 Flow Domain Geometry

The flow domain is in the shape of a halved cylinder (lengthwise), with a rounded edge at the inlet as shown in Fig 10 below. Its overall diameter is 50 meters and is 50 meters in length from inlet to outlet. This geometry selection is utilized to limit the number of elements and nodes generated during the meshing process. A cuboid-shaped domain would include trivial volumes at the outer edges of the geometry (in the flow direction) that would not add accuracy to the result. The wing's geometry is imported to ANSYS after modelling it in external software and is then cut out of the domain using a subtractive Boolean operation, leaving only the wing's wall boundaries. This allows for less mesh generation, as we are not analyzing the wing structure but the flow around its faces.

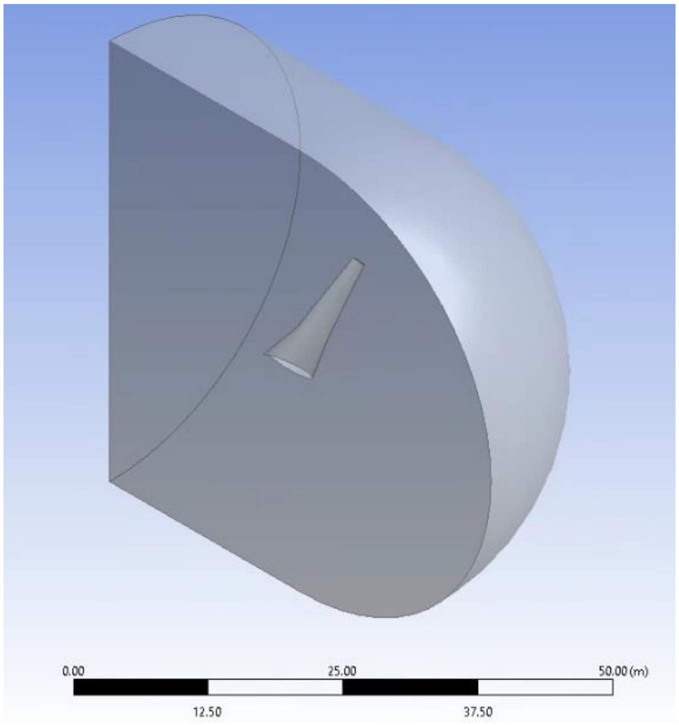

Figure 10. Simulation Computational Domain Geometry

The model also includes a smaller intermediate domain which is used as a meshing body of influence. This is used to create a more refined mesh in the region local to the wing surfaces to capture an accurate result, including the effects of flow stagnation and separation. Special meshing considerations were given to the sharp trailing edge of the wing, as it is modelled with a very small radius to avoid forcing the meshing program to evaluate sharp edges. The mesh for the base A320 wing is shown in Figure 11 after all sizing parameters are applied and generated.

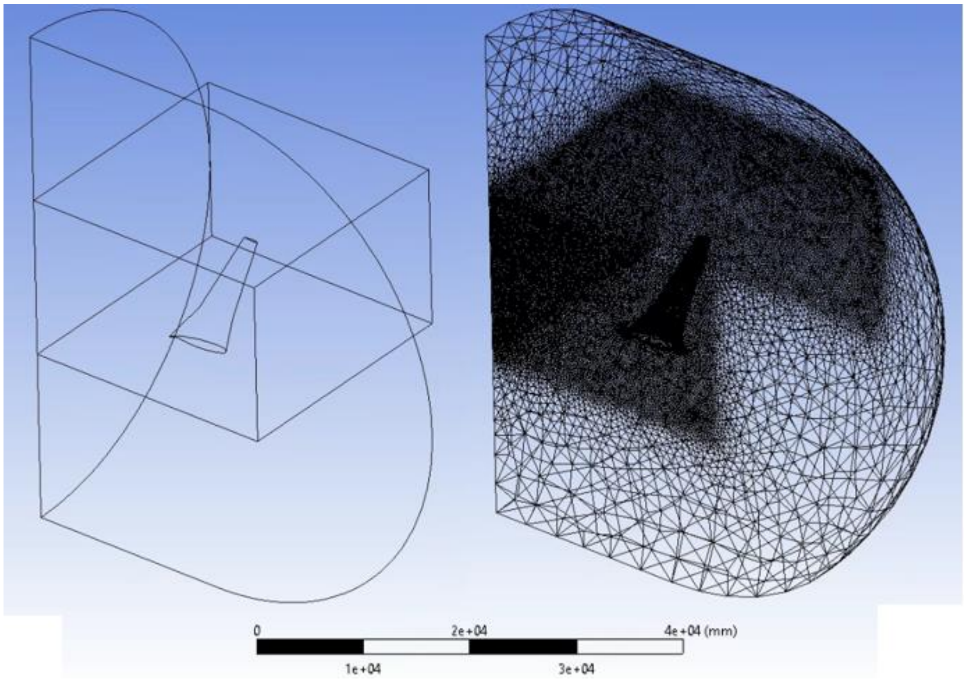

Figure 11. Body of Influence and Meshed Domain

This mesh was generated using several sizing parameters on the wing's surfaces, including face and edge sizing metrics as well as inflation layers of multiple magnitudes. These selections were maintained across all simulations with minor adjustments for varying geometries. Table 2 shows the sizing parameters exercised in this study.

Table 2. Mesh Sizing Selections

Geometry	Specification
Primary domain	~3500 mm
Intermediate domain (body of influence method)	250 mm
Wing upper / lower surfaces (face sizing)	250 mm
Leading edge (edge sizing)	25 mm
Trailing edge (edge sizing)	5 mm
Sharp intersections (edge sizing)	1 mm

3.2.4 Output Parameters and Post Processing

Initialization and setup parameters for the simulation were also held constant. Reference values such as area and length as defined by ANSYS were set as the planform area and wingspan to calculate the lift and drag coefficients as defined for airfoils. The expressions used in the program to determine the lift and drag coefficients, C_l and C_d are shown in Eq. (12), Eq. (13), and Eq. (14).

$$C_l = \frac{L}{\frac{1}{2}A\rho v^2} = \frac{L}{q\,A} \tag{12}$$

$$C_d = \frac{D}{\frac{1}{2}A\rho v^2} = \frac{D}{q\,A} \tag{13}$$

$$q = \frac{\rho v^2}{2} \tag{14}$$

In these expressions, L is lift force, D is drag force, A is planform area of the wing, and q is dynamic pressure. The model was then initialized at the inlet for each case, and the simulation was set to run for a maximum of 200 iterations. A convergence magnitude of 10^{-6} was included to ensure an accurate, converged experimental solution. Figure 12 shows the boundary conditions selected for the simulations.

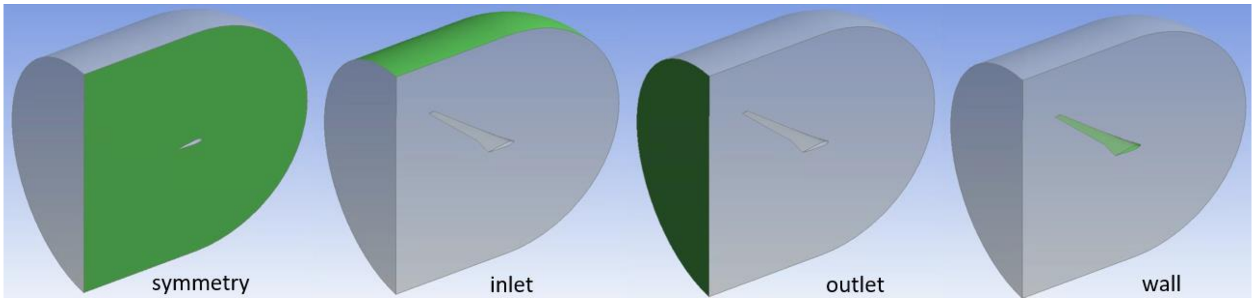

Figure 12. Simulation Domain Boundary Selections

The post processing software CFD-Post was utilized to generate visualized results for each simulation such as pressure contours, velocity swirl, turbulence kinetic energy, and the geometry of the vortex core region produced by the wing. This software was also used to determine where the CoP is located for the wings. This point was utilized during physical experimentation to locate the mounting points for the lift-force load cells. To execute this, a user-defined expression was defined as shown in Eq. (15).

$$CP_{X,Y,Z} = areaInt([X,Y,Z]*Pressure)@wing \,/\, areaInt(Pressure)@wing \qquad (15)$$

This function sums the pressures on the walls of the wing in each coordinate direction and then divides that result by the total pressure exerted on the entire wall region from all directions. This results in each coordinate of the CoP, or where the average location of the pressure variation occurs. For the bare supercritical and conventional wings, the coordinates (X, Y, Z) were found to be (2.868, 0.680, 5.536) (m) and (2.705, 0.660, 5.600) (m), respectively.

3.3 Wind Tunnel Experimentation

3.3.1 Tunnel Parameters

The experimental setup for this study was used to collect the lift and drag forces produced by scaled wing-winglet combinations in a subsonic, open-loop wind tunnel. The wind tunnel utilized during this study (Fig 13) can produce flows with a maximum velocity of approximately 13 m/s before unsteady vibration occurs. The flow is pushed through a rectangular outlet with a hydraulic diameter of 0.61 m. This circulation is controlled via a variable frequency drive (Fig 14) which allows for the modulation of the tunnel's fan motor speed by changing the frequency of the AC power supplied to it. For this testing, a flow velocity of 12 m/s (approximately 36 Hz on the wind tunnel VFD) was selected to remain safely under the maximum threshold of the wind tunnel. In Table 3, various flow velocities and their respective VFD frequencies are shown for reference.

Figure 13. Georgia Southern University Subsonic Wind Tunnel

Figure 14. VFD Wind Tunnel Controller

Table 3. VFD Frequencies to Flow Velocities

Frequency (Hz)	3.07	6.13	9.20	12.27	15.06	18.07	21.37	24.35	27.33	30.36	33.40	36.00
Velocity (m/s)	1	2	3	4	5	6	7	8	9	10	11	12

3.3.2 Model Preparation

The wings and accompanying wing-tip devices were 3D printed with polyethylene terephthalate glycol (PETG); a common type of polyester used as filament for fused deposition modeling (FDM) printers. This manufacturing method leaves very small layer lines which create a texture on the surface of components (Fig 15), which was overcome by sanding and priming the wings/winglets with aerosol filler-primer until the surface was smooth (Fig 16). The winglets were attached with several small neodymium magnets which were embedded within the tip of the wings as well as the root of each winglet as shown in Fig 17.

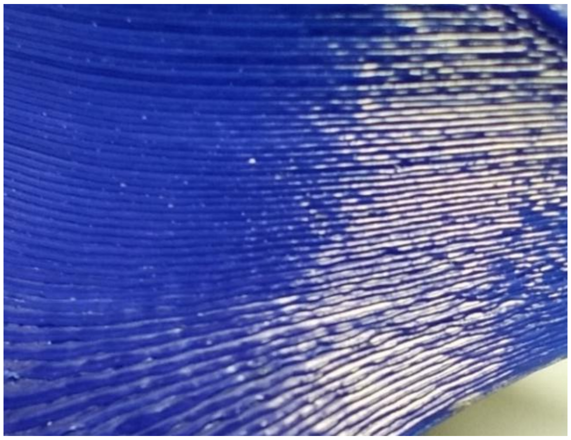

Figure 15. Layer Lines Characteristic of FDM Printing

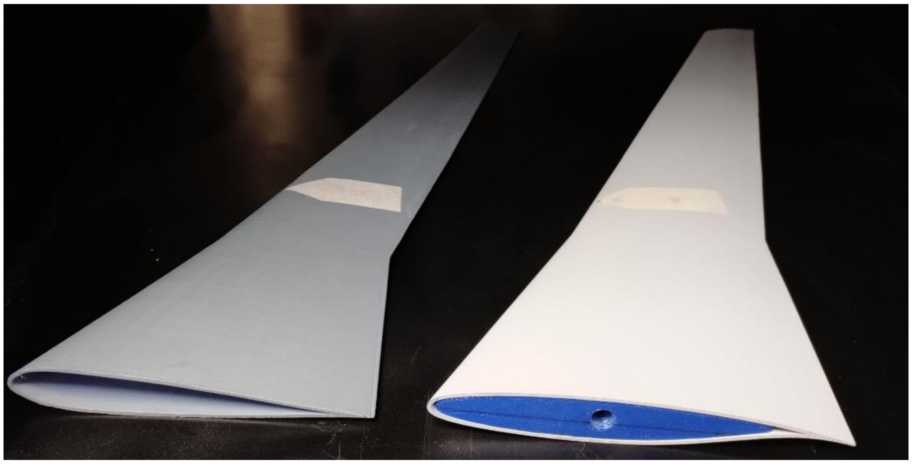

Figure 16. Finished Wing Surfaces

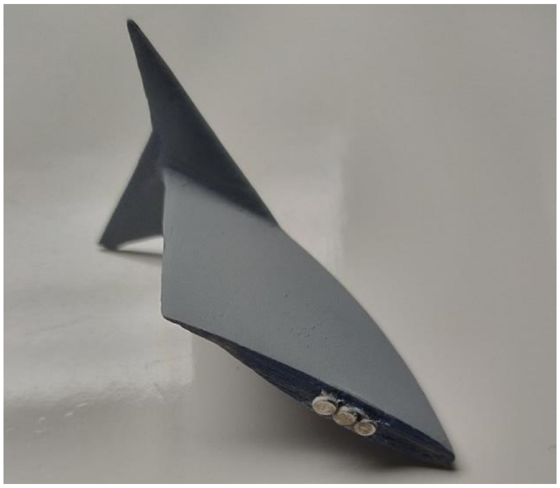

Figure 17. Winglet Magnetic Mount Application

The prototype wings, each having a span of 15 meters, were scaled to 0.43 m in length from root to tip, preventing the tip of the model wing and accompanying winglets from experiencing boundary layer affects derived from the walls of the wind tunnel's test section. The MACs of the scaled wings are 130.10 mm (wing composed of supercritical airfoils) and 113.89 mm (wing composed of traditionally cambered airfoils). The tests were run at sea-level elevation in laboratory conditions, so average room-temperature air properties were assumed (density of 1.225 kg/m^3, dynamic viscosity of 1.825x10^{-5} m^2/s). This resulted in approximated Reynolds numbers of 1.05x10^5 for the supercritical wing and 9.17x10^4 for the traditionally cambered wing.

3.3.3 Aerodynamic Similarity Criteria

Due to testing equipment constraints and the high velocity flows that plane wings experience, matching the Reynolds number was not possible during physical experimentation. Analysis of similarity criteria through dimensional analysis of geometric, kinematic, and dynamic principles revealed these limitations within the study. Geometrical similarity required linear scaling in all coordinate directions as well as the preservation of all flow angles and directions, which was neatly observed. Kinematic similarity, or the similarity of time scales, revealed through the Froude Number relationship that a wind tunnel speed of 39.1 m/s would have been required to match the prototype and model's time scaling accurately. Equation (16) shows the expression used to evaluate the Froude Number.

$$FR_p = \frac{V_p^{\,2}}{gL_p} = \frac{V_m^{\,2}}{gL_m} = FR \tag{16}$$

The third parameter, dynamic similarity, was not observable due to the inequality found in the previous principles. This regards the scaling of forces, requiring equality between the respective Reynolds and Mach numbers of the prototype and model. This scaling of forces is determined by the following relationship in Eq. (17).

$$F_p = F_m(\frac{\rho_p}{\rho_m})(\frac{V_p}{V_m})^2(\frac{L_p}{L_m})^2 \tag{17}$$

However, the magnitudes of lift and drag forces and their coefficients should provide valuable insight into wing-winglet efficiency, corroborating the full-scale simulative work done in ANSYS by allowing for the identification of trends in lift and drag data.

3.3.4 Testing Apparatus

Several of the components of the testing apparatus were also manufactured using the same 3D printing methods, including the mount which interfaces with the bottom surface of the wing (Appendix A) in the wind tunnel. It was designed to facilitate effortless replacement of wing structures while maintaining rigid support during testing. This coupler is secured via hidden M3 screws at the wing's CoP (x and y coordinates) as determined by the CFD simulations of the base wing. Its structure is composed of NACA 0012 airfoil profiles to help reduce extraneous vorticity near the wing's bottom surface as much as possible. A rotating joint was incorporated into the coupler as well to allow for the adjustment of the wing's angle of attack from 0° to 8° via marked indexing. This coupler is attached to two machined aluminum posts, which are then threaded into two s-type load cells responsible for measuring the lift forces produced by the airfoil. This entire assembly is fixed on a length of aluminum bar stock which is supported above and below by low-friction roller bearings, allowing only for translation in the direction of flow. This allows for a third s-type load cell to read drag forces via the lateral forces transmitted through the entire structure from the wing and winglet exposed to the flow in the tunnel above. Figures 18-21 below show a schematic of this setup and its physical implementation. The wing is positioned in such a way that the root profile is very close to the wall of the tunnel, avoiding the formation of vorticity as is produced by lift-induced drag at the wing's tip. However, no contact is made between the model and the tunnel's walls to prevent lift and drag readings from being impacted.

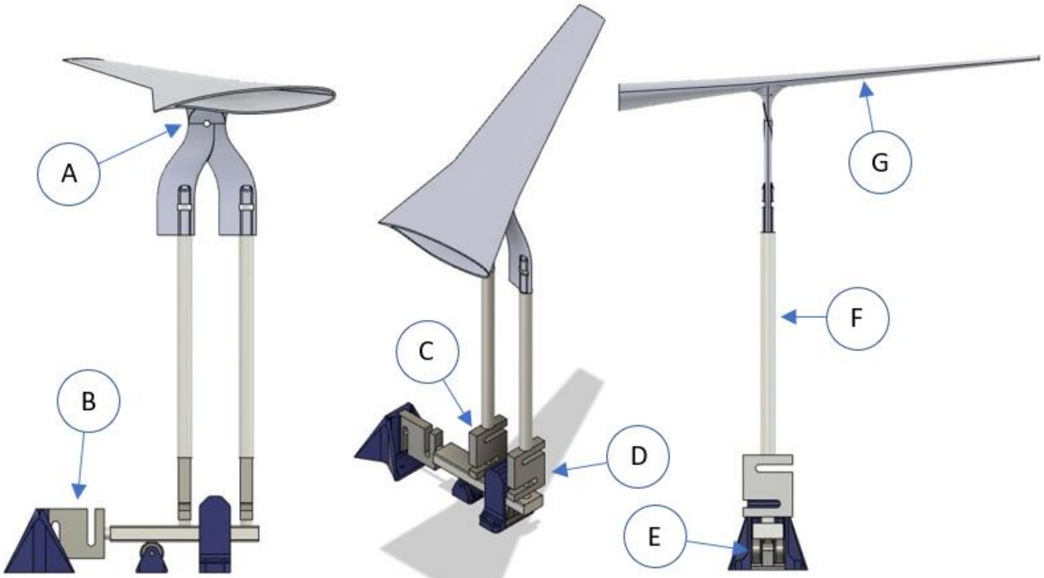

Figure 18. Lift and Drag Load Cell Apparatus Schematic. (A) AoA Adjustment Pivot. (B) Drag Load Cell. (C) Lift Load Cell #1. (D) Lift Load Cell #2. (E) Roller Bearings. (F) Aluminum Support Posts. (G) Model Wing.

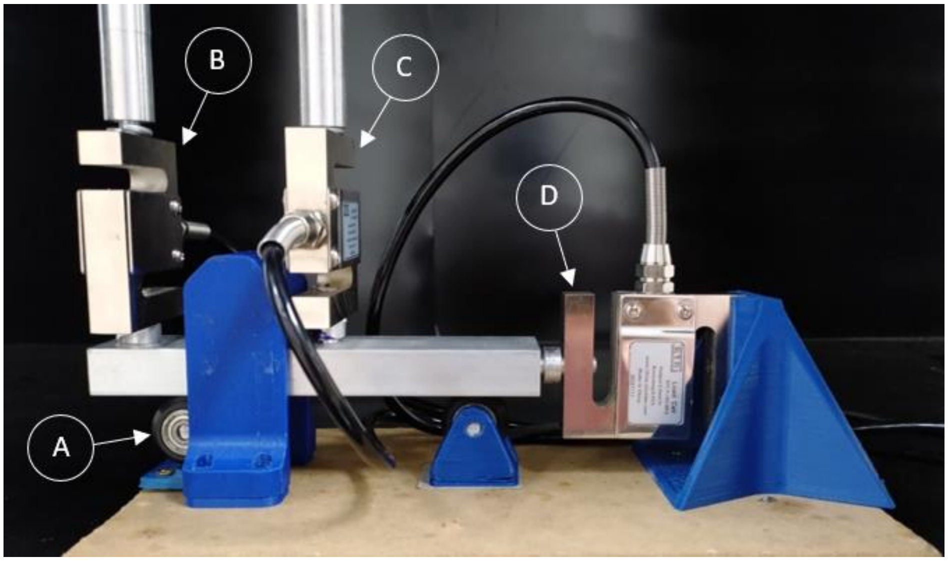

Figure 19. Load Cells Attached to Testing Apparatus. (A) Roller Bearings. (B) Lift Load Cell #2. (C) Lift Load Cell #1. (D) Drag Load Cell.

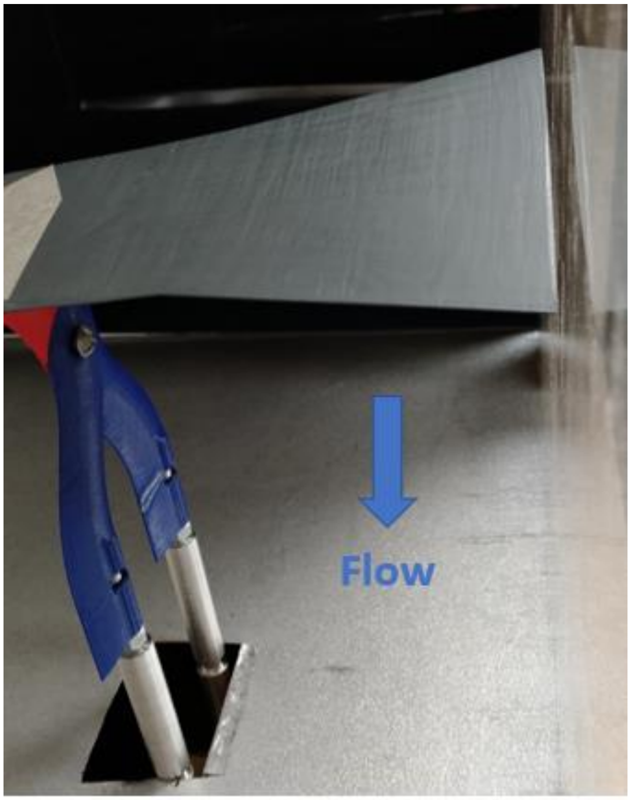

Figure 20. Traditional Wing Mounted in Tunnel

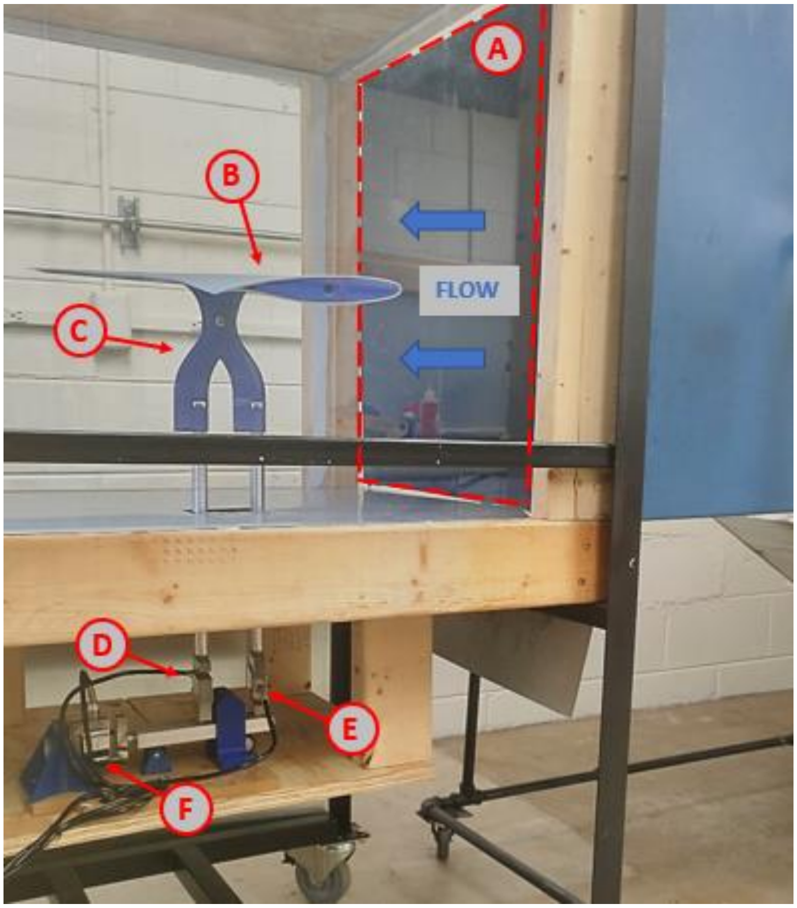

Figure 21. Supercritical Wing Mounted in Tunnel. (A) Wind Tunnel Outlet. (B) Wing Model. (C) Wing Mount. (D) Lift Load Cell #1. (E) Lift Load Cell #2. (F) Drag Load Cell.

3.3.5 Data Acquisition Specifications and Calibration

The implemented load cells can measure up to 5 kg in either the compression or tensile direction with a full Wheatstone bridge incorporated inside each load cell (Fig 22). The analog output is converted to a digital signal and amplified with a gain of 32x via an HX711 ADC breakout board which is then read by an Arduino Mega 2560 microprocessor (Fig 23). The code used for this application utilized a non-blocking timer that was set to record the output from each load cell every 250 milliseconds. Data was collected from the Arduino serial monitor window once the flow reached the desired velocity. For each wing-winglet combination at each angle of attack, 15 samples of lift and drag values were taken and averaged to reduce the influence of turbulence or structural vibration on the readings. Each load cell was calibrated individually using a series of brass weights in 50g graduations before being incorporated into the testing apparatus. This was done to determine the characteristic curve for each, allowing for the DAQ outputs to be translated directly to specific loading values to identify lift and drag forces when using the finalized setup (Fig 24).

Figure 22. 5 Kg S-Type Load Cell

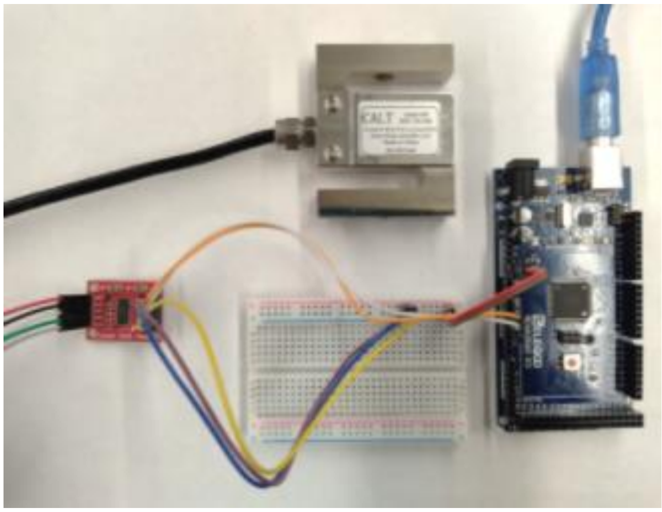

Figure 23. Arduino Mega 2560 and HX711 Data Acquisition Setup

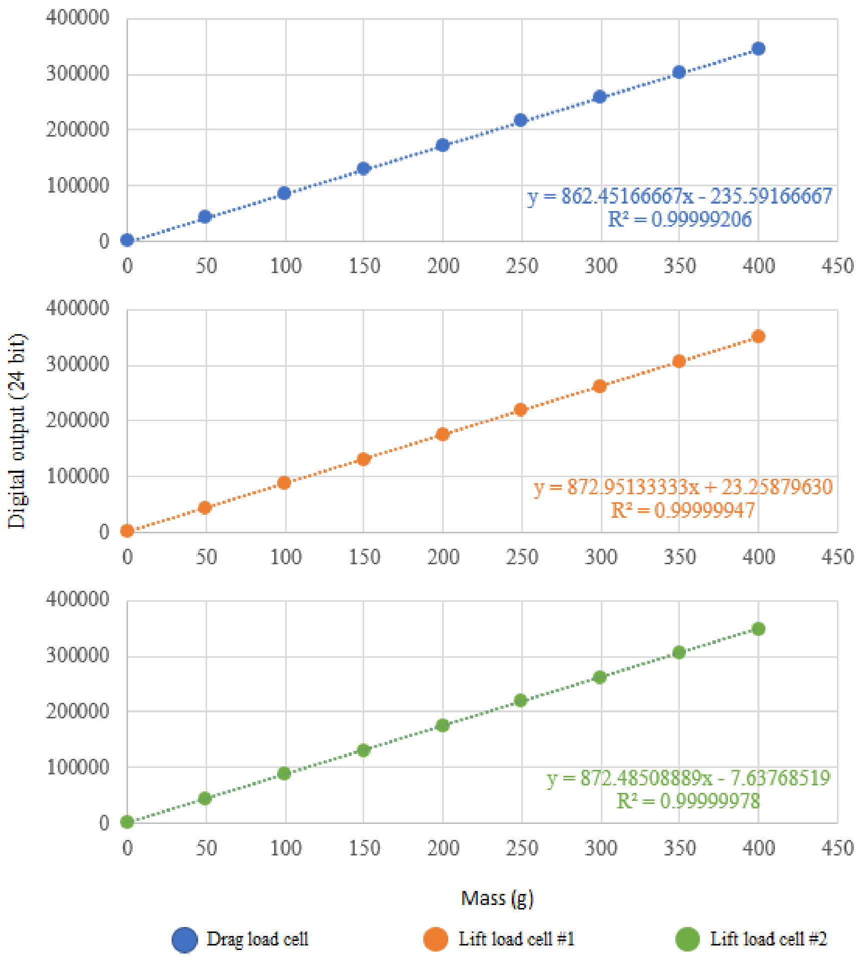

Figure 24. Load Cell Calibration Curves

This sampling procedure resulted in sufficiently high r-square values during linear regression analysis, all having very high linearity. All y-intercepts of these characteristic curves are close to zero at no-load conditions, allowing the author to conclude with reasonable confidence that there are no major manufacturer defects or zeroing issues with the DAQ equipment or load cells. Following characterization, a baseline reading of the apparatus was necessary to identify the magnitude of lift and drag force produced by its own structure at each AoA before a wing is applied. By identifying this offset, a more accurate result closely representing the capabilities of the model wings can be identified. Several readings were taken at each angle of attack at the tunnel testing velocity of 12 m/s (Fig 25). These results were then averaged to obtain an offset value to subtract from readings of the various wing and winglet combinations. In doing so, the lift and drag forces generated solely by the wings and winglets can be identified, barring any outside influence on the data from the forces generated by the test apparatus itself. Figure 26 outlines this process, while the averaged lift and drag force offsets are identified in Table 4.

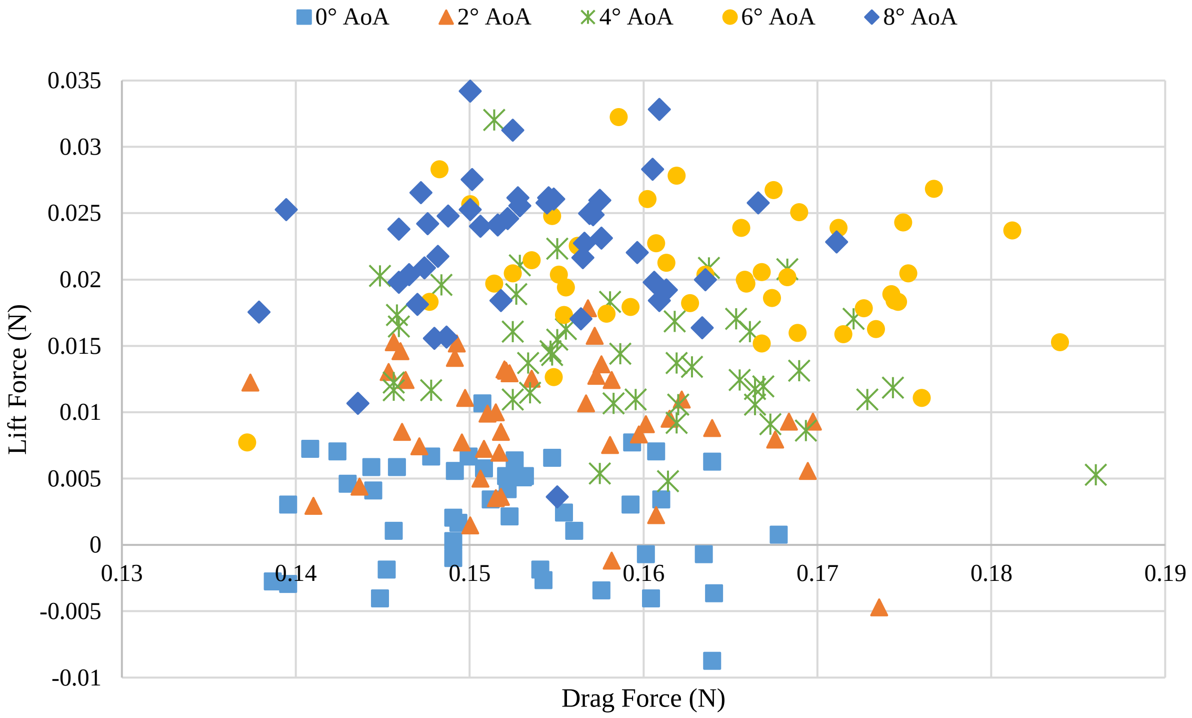

Figure 25. Load Cell Offset Measurements (No Wing Attached)

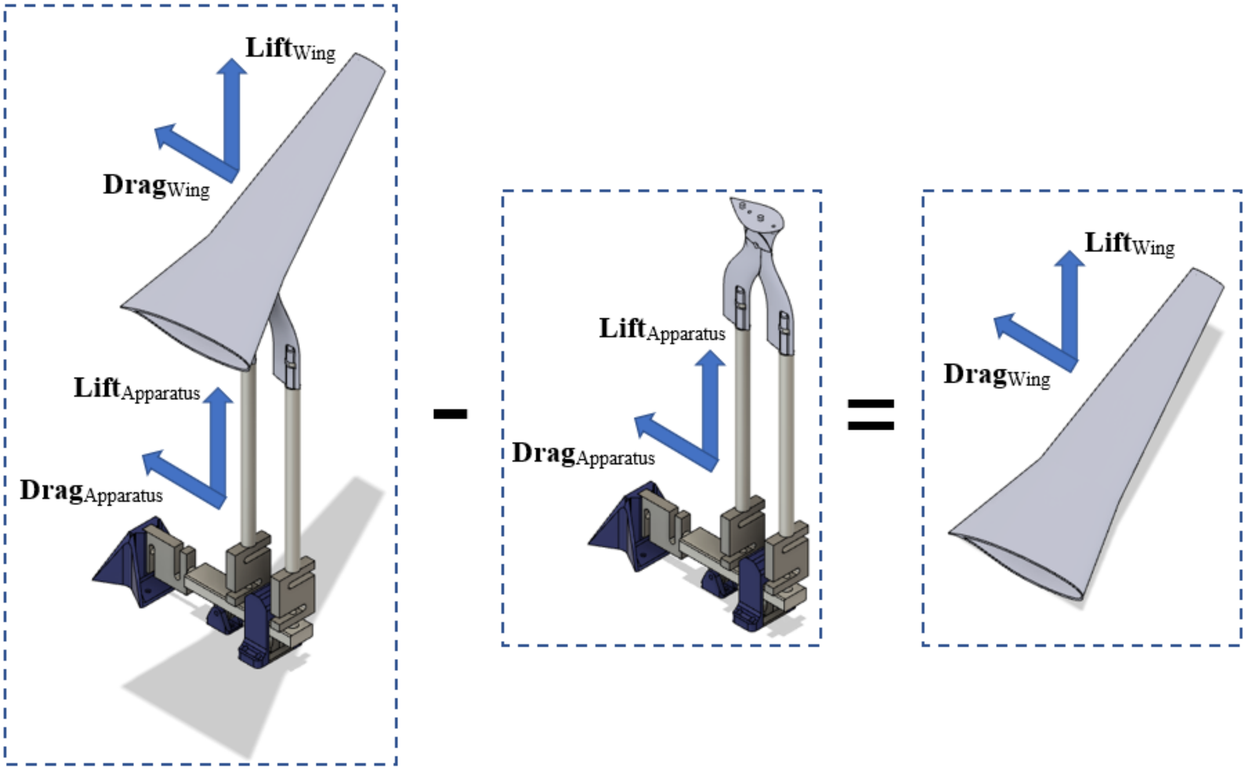

Figure 26. Apparatus Lift and Drag Offset Application

Table 4. Averaged Apparatus Lift and Drag Force Offsets

Angle of Attack (AoA)	Lift Force (N)	Drag Force (N)
■ 0° AoA	0.002	0.152
▲ 2° AoA	0.009	0.154
✳ 4° AoA	0.014	0.159
● 6° AoA	0.020	0.164
◆ 8° AoA	0.023	0.153

CHAPTER 4

RESULTS AND ANALYSIS

4.1 Computational Fluid Dynamics

4.1.1 Numerical Results

The solution metrics for the simulative portion of this study include plots generated from data taken from ANSYS Fluent report definitions. Figures 27 and 28 represent the lift and drag forces output by the simulation for both wing designs. Following these results, the lift and drag coefficients as well as the ratios between the two were calculated to show trends in overall aerodynamic efficiencies of each wing-winglet combination (Fig 29-32). This ratio of coefficients is one example of an industry-standard practice utilized to define the effectiveness of an airfoil or wing by examining its lift and drag production. To optimize a wing design or select the optimal winglet for an elevated level of aerodynamic efficiency, a higher C_l / C_d ratio is desired. By this principle, the best wing and winglet combination can be identified by the pairing with the highest magnitude of lift and lowest magnitude of drag, resulting in the highest C_l / C_d ratio.

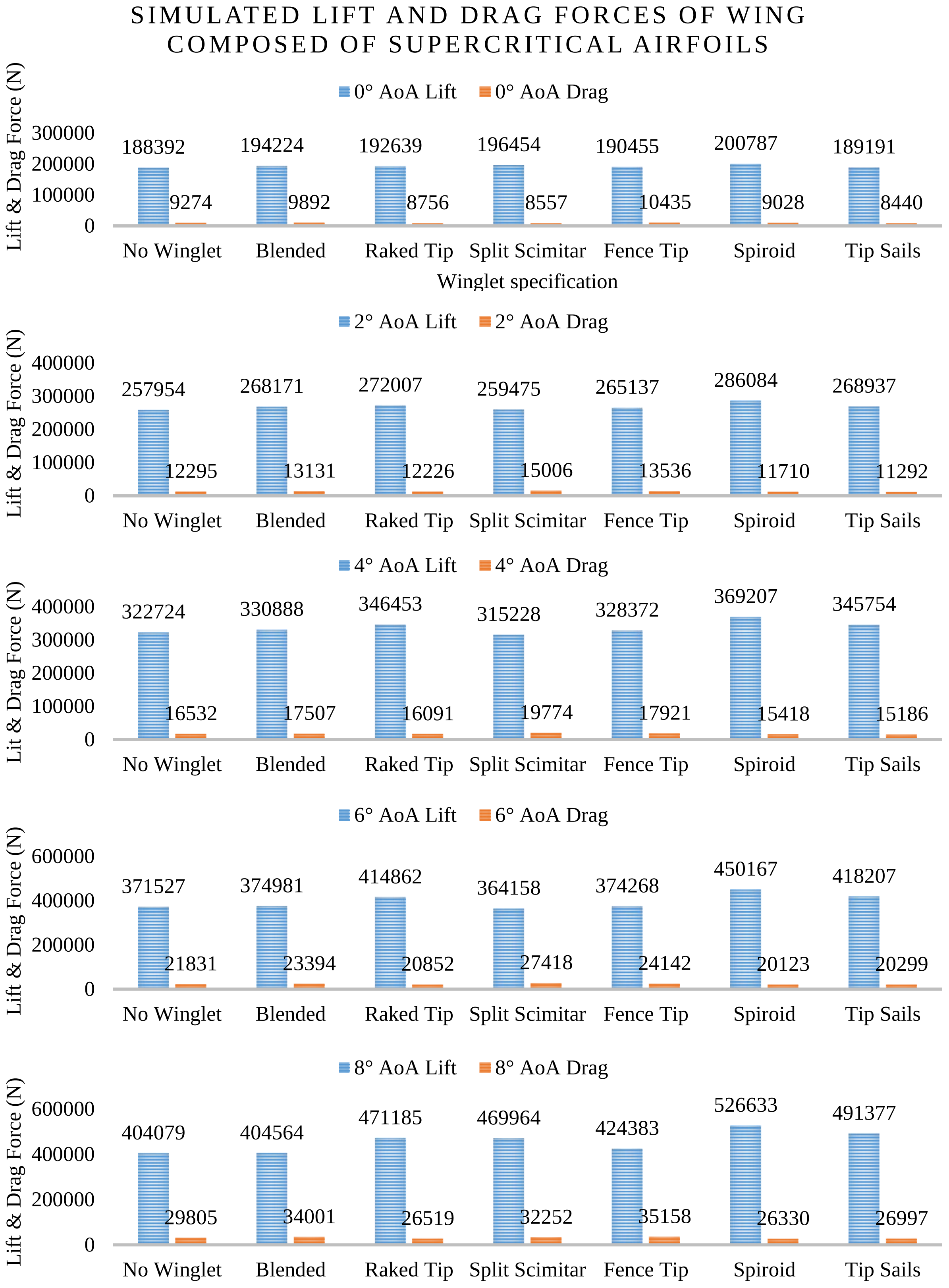

Figure 27. Simulated Lift and Drag Forces of Wing Composed of Supercritical Airfoils

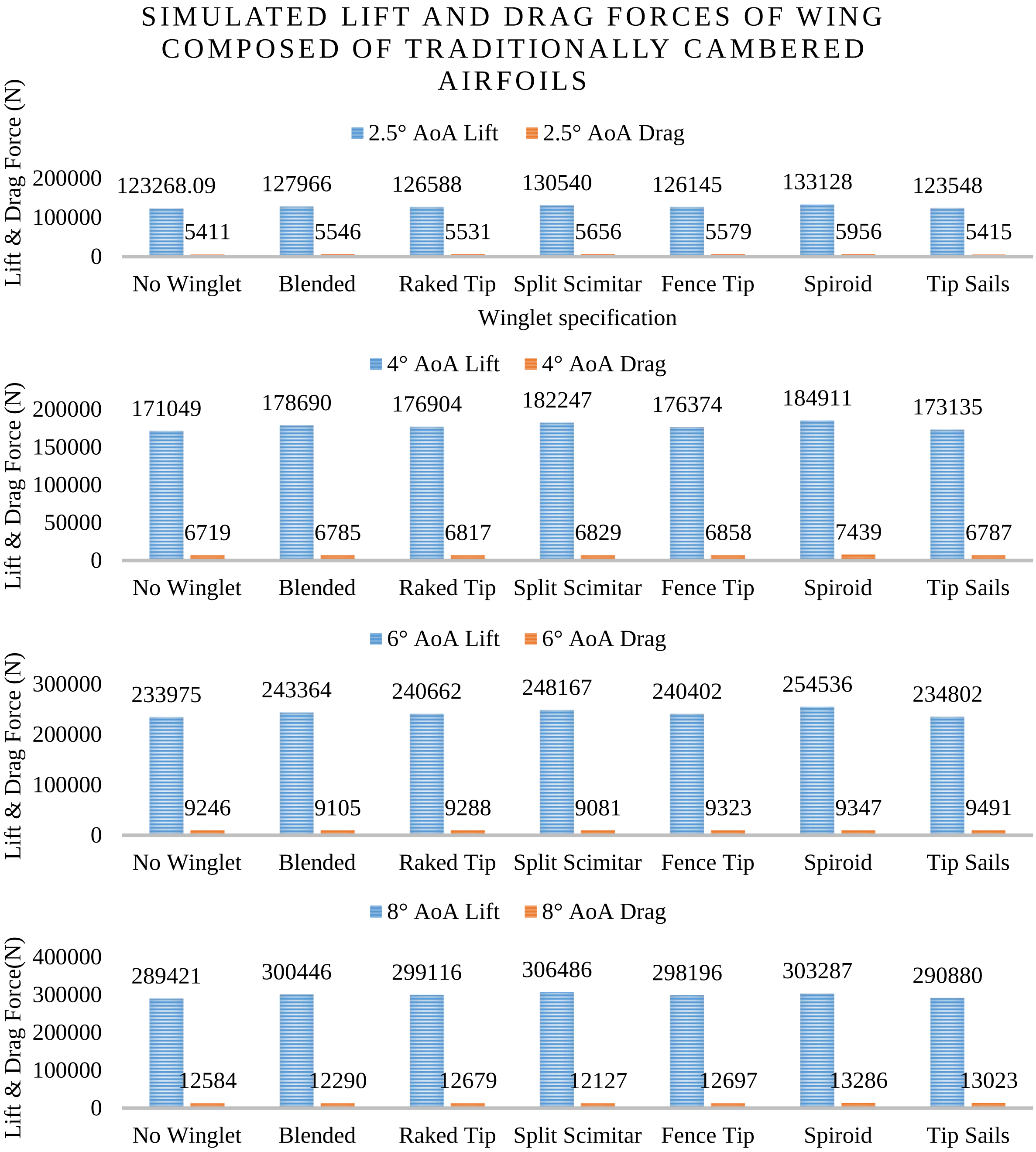

Figure 28. Simulated Lift and Drag Forces of Wing Composed of Traditionally Cambered Airfoils

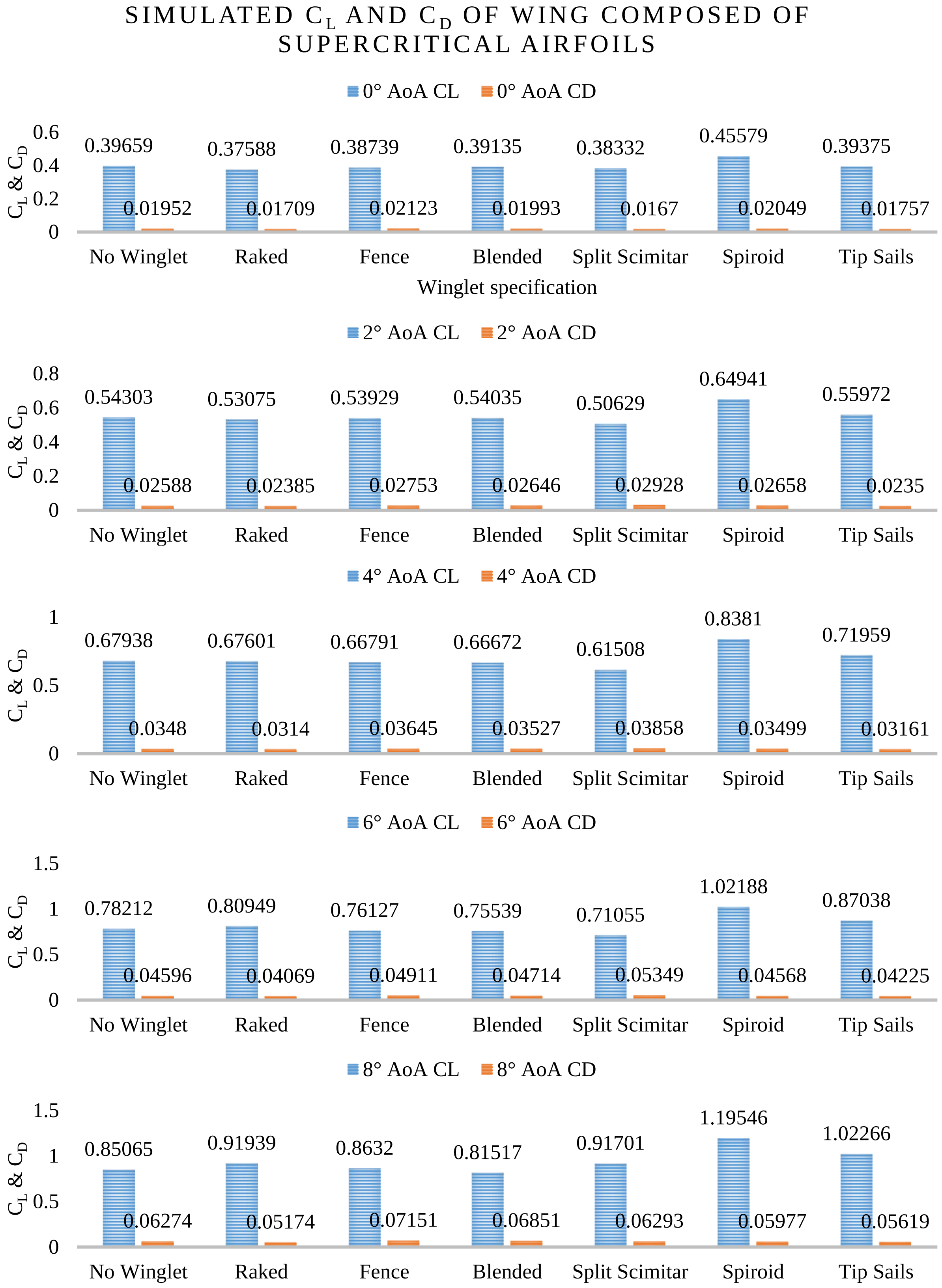

Figure 29. Simulated C_l and C_d of Wing Composed of Supercritical Airfoils

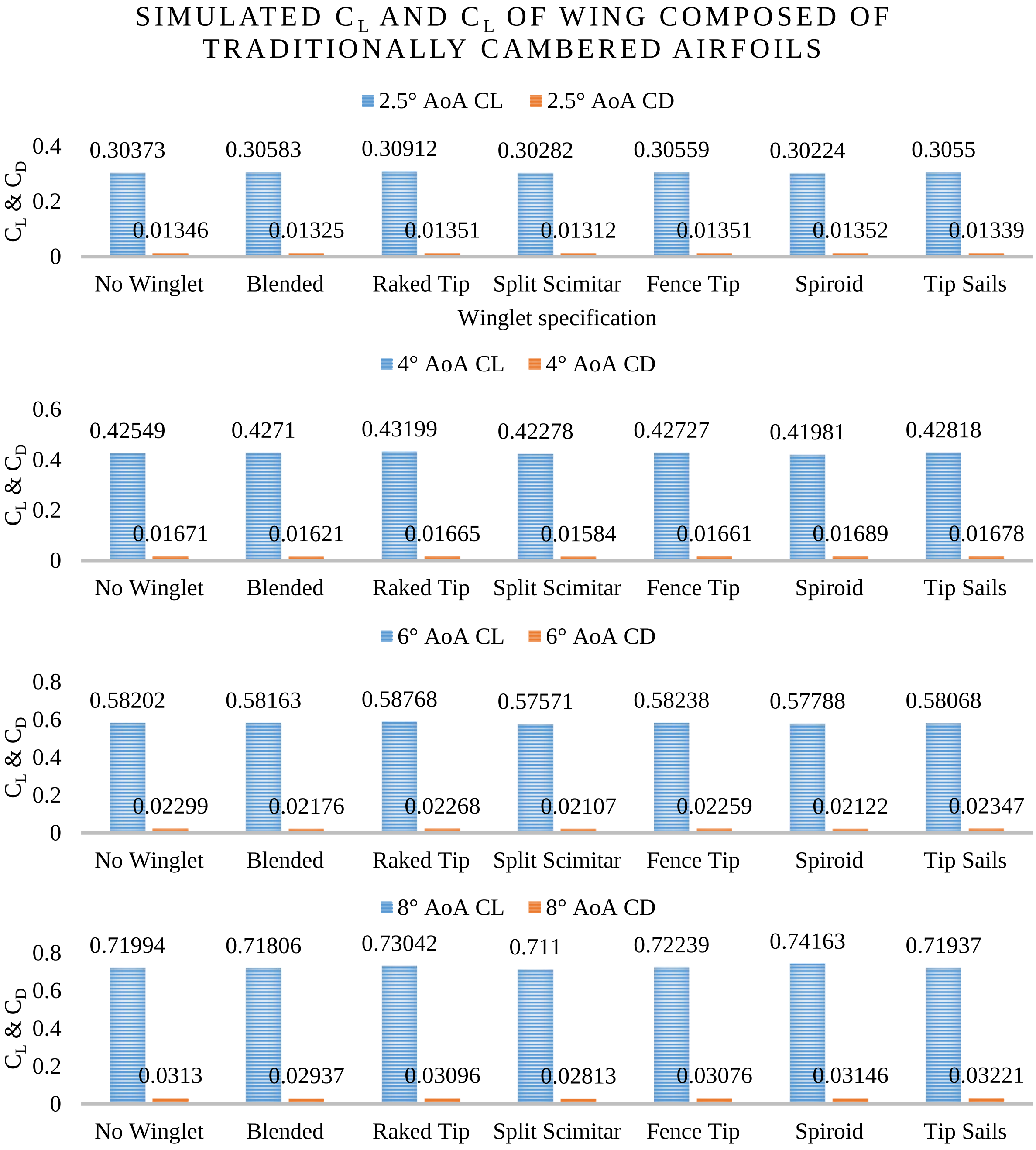

Figure 30. Simulated C_l and C_d of Wing Composed of Traditionally Cambered Airfoils

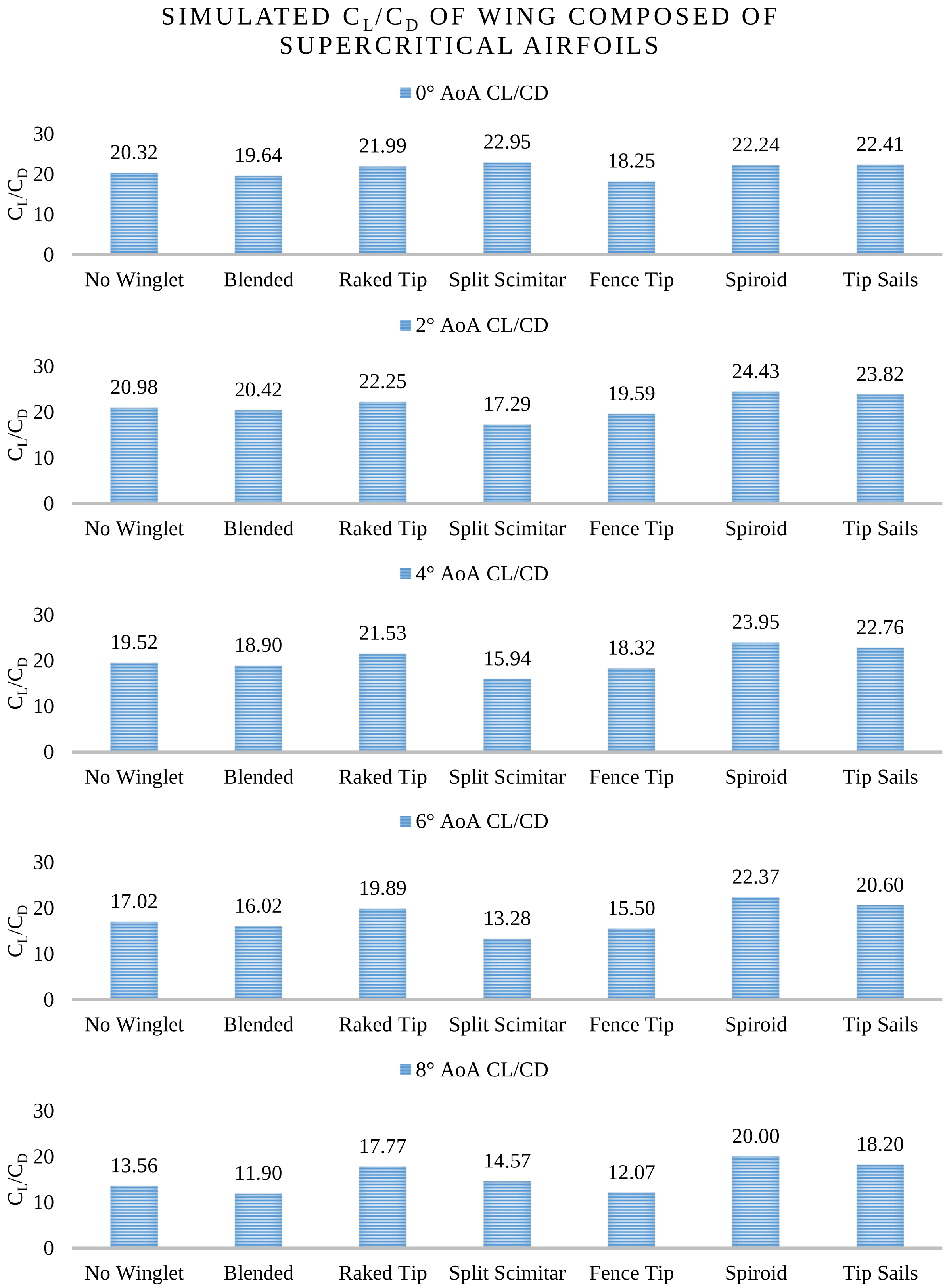

Figure 31. Simulated C_l / C_d of Wing Composed of Supercritical Airfoils

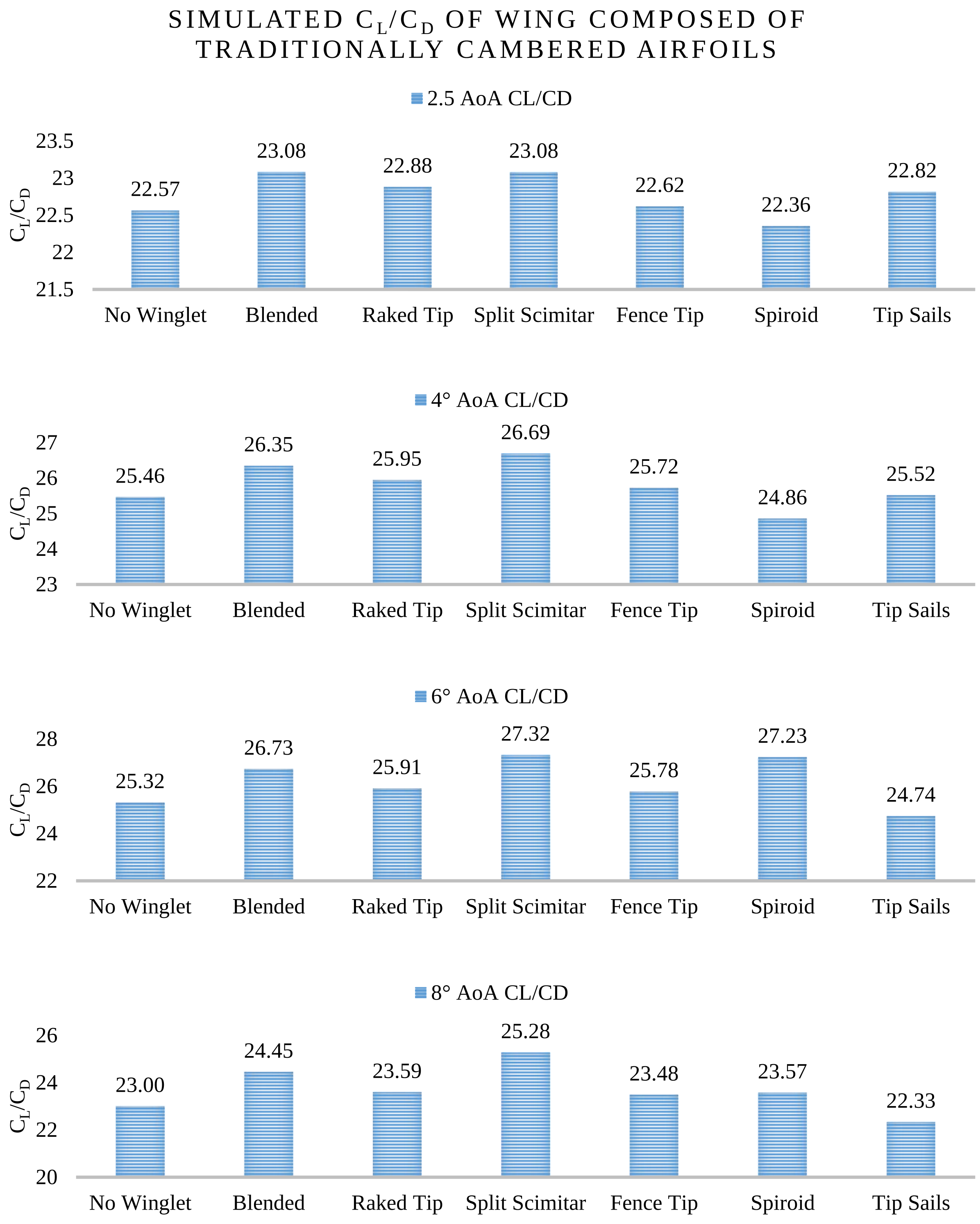

Figure 32. Simulated C_l / C_d of Wing Composed of Traditionally Cambered Airfoils

4.1.2 Visual Vorticity Definition

Following the numerical results from the simulative portion of this study, visual representations of the vorticity produced help to indicate how each wing-winglet combination relocate the vorticity responsible for induced drag at the wingtips (Fig 33-46). For the purposes of these results, an angle of attack of 2° for the supercritical wing and 6° for the traditionally cambered wing was chosen for velocity curl visualization based on their similar lift force production at those angles. This post-processing method shows the curl rate of the lift-induced drag vorticity as well as its location and spread, which can help to substantiate the wing/winglet combinations as described by the C_l / C_d ratio. Maximum values of velocity curl are shown in Tables 5 and 6 corresponding to wing type.

4.1.2.1 Supercritical Wing Velocity Curl

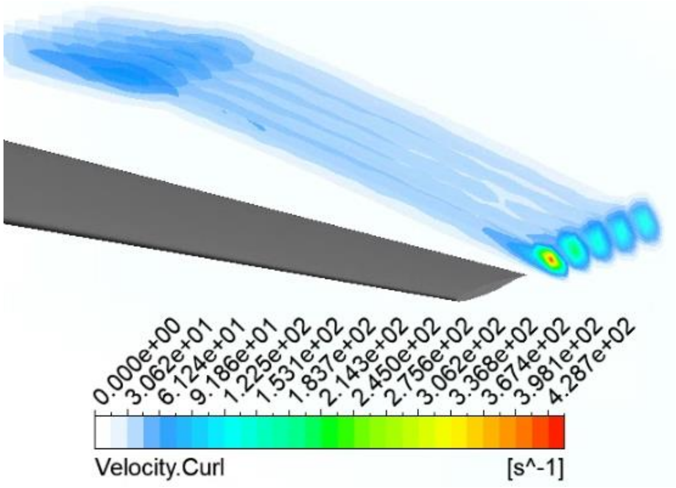

Figure 33. Supercritical Wing, No Winglet Velocity Curl

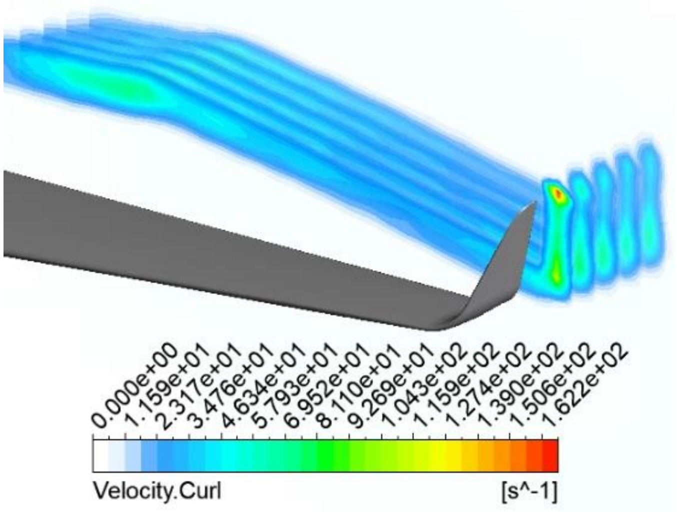

Figure 34. Supercritical Wing, Blended Winglet Velocity Curl

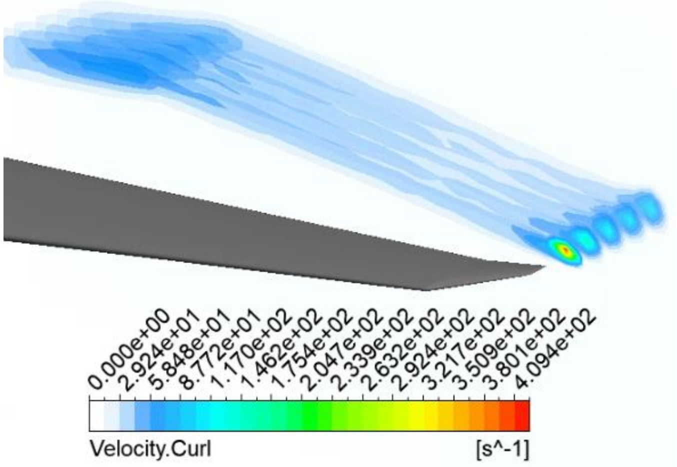

Figure 35. Supercritical Wing, Raked Winglet Velocity Curl

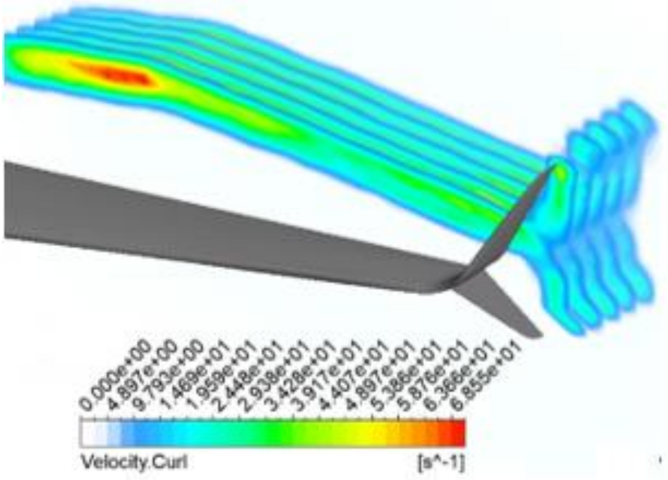

Figure 36. Supercritical Wing, Split Scimitar Winglet Velocity Curl

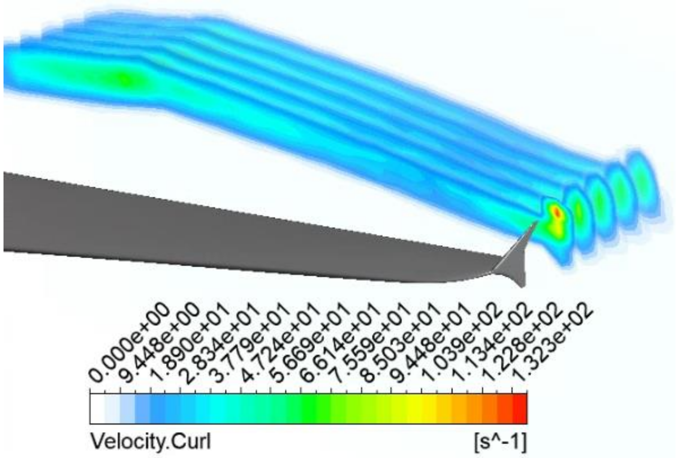

Figure 37. Supercritical Wing, Fence Winglet Velocity Curl

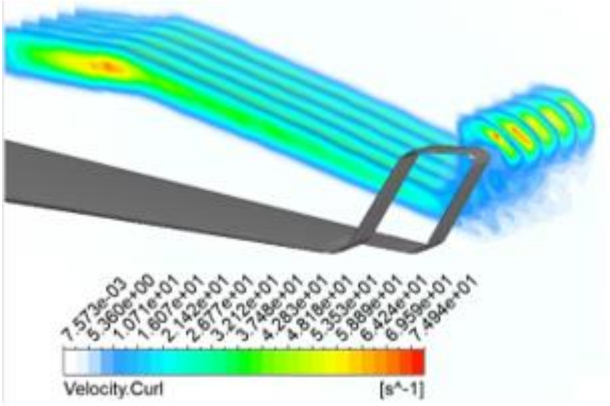

Figure 38. Supercritical Wing, Spiroid Winglet Velocity Curl

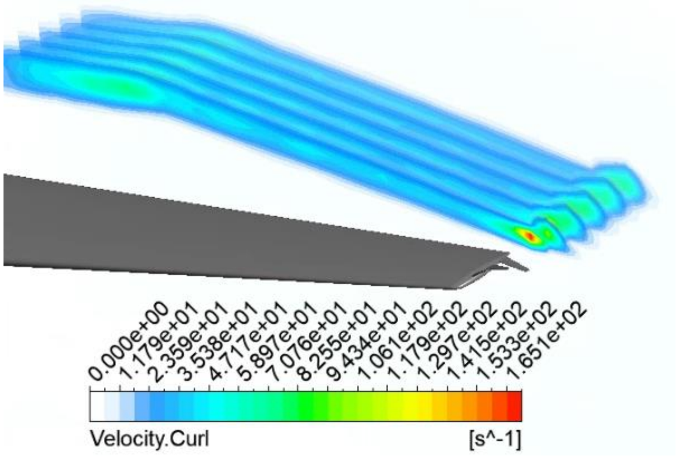

Figure 39. Supercritical Wing, Tip Sails Velocity Curl

Table 5. Supercritical Wing Maximum Velocity Curl Magnitudes

Winglet Configuration	Velocity Curl Magnitude (s^{-1})
No winglet	428.7
Blended	162.2
Raked	409.4
Split Scimitar	68.5
Fence	132.3
Spiroid	74.9
Tip Sails	165.1

4.1.2.2 Traditionally Cambered Wing Velocity Curl

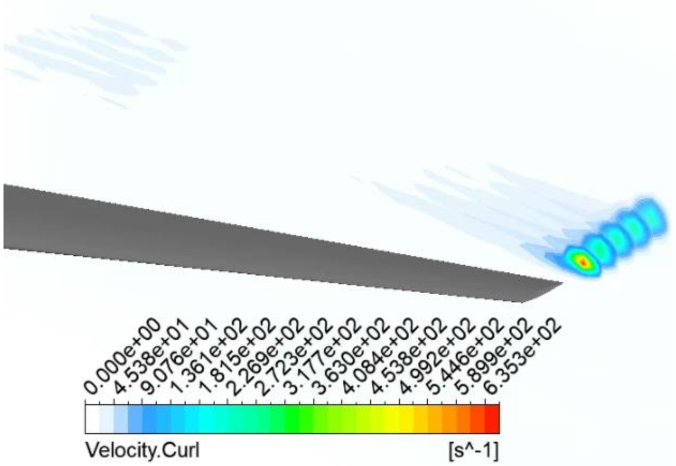

Figure 40. Traditional Wing, No Winglet Velocity Curl

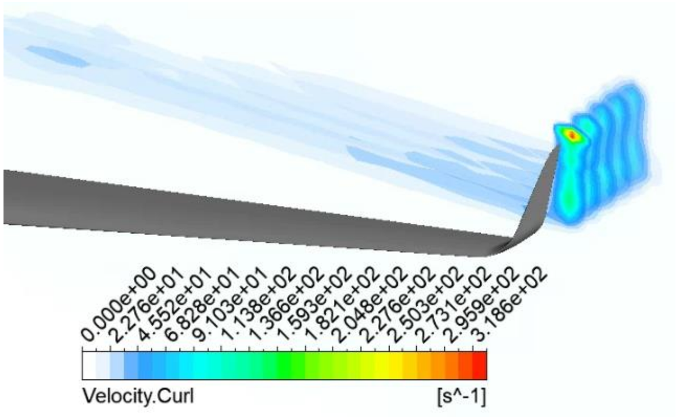

Figure 41. Traditional Wing, Blended Winglet Velocity Curl

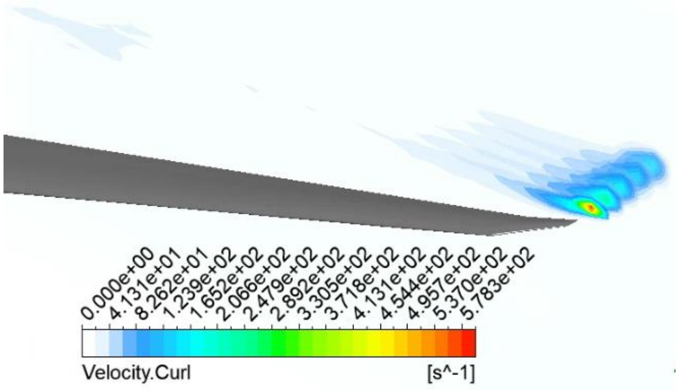

Figure 42. Traditional Wing, Raked Winglet Velocity Curl

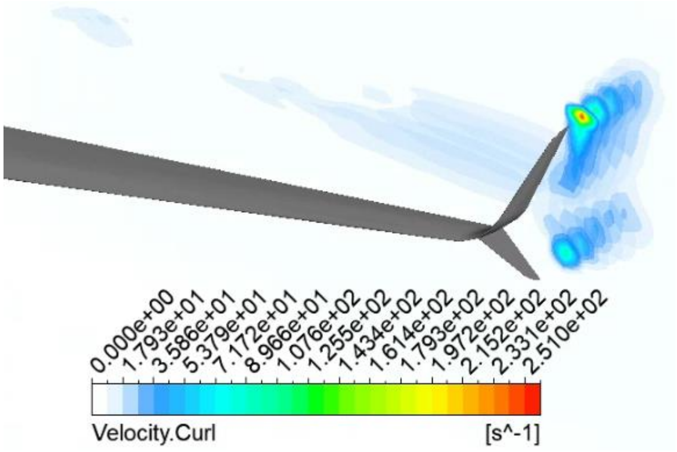

Figure 43. Traditional Wing, Split Scimitar Winglet Velocity Curl

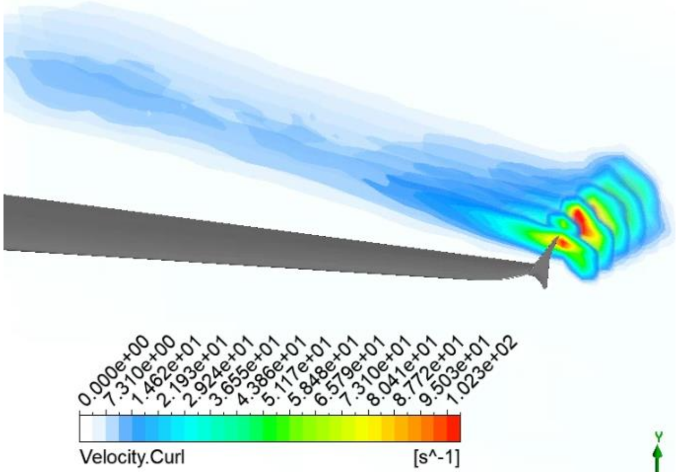

Figure 44. Traditional Wing, Fence Winglet Velocity Curl

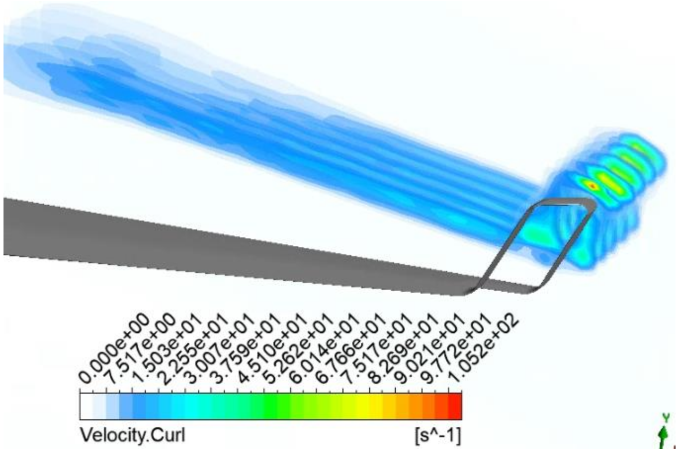

Figure 45. Traditional Wing, Spiroid Winglet Velocity Curl

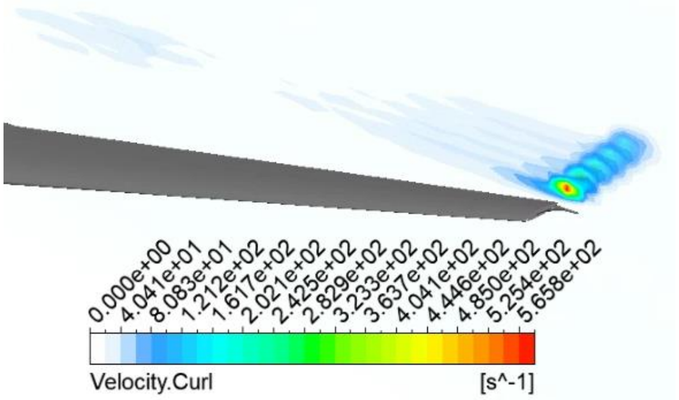

Figure 46. Traditional Wing, Tip Sails Velocity Curl

Table 6. Traditionally Cambered Wing Maximum Velocity Curl Magnitudes

Winglet Configuration	Velocity Curl Magnitude (s^{-1})
No winglet	635.3
Blended	318.6
Raked	578.3
Split Scimitar	251.0
Fence	102.3
Spiroid	105.2
Tip Sails	565.8

4.2 Results of Wind Tunnel Experimentation

The experimental test setup was designed to collect lift force and drag forces, which were recorded and used to manually calculate lift and drag coefficients and the ratios between the two. This information was plotted in the same manner as the simulative data, and trends were observed. Figures 47-52 show the tabulated findings.

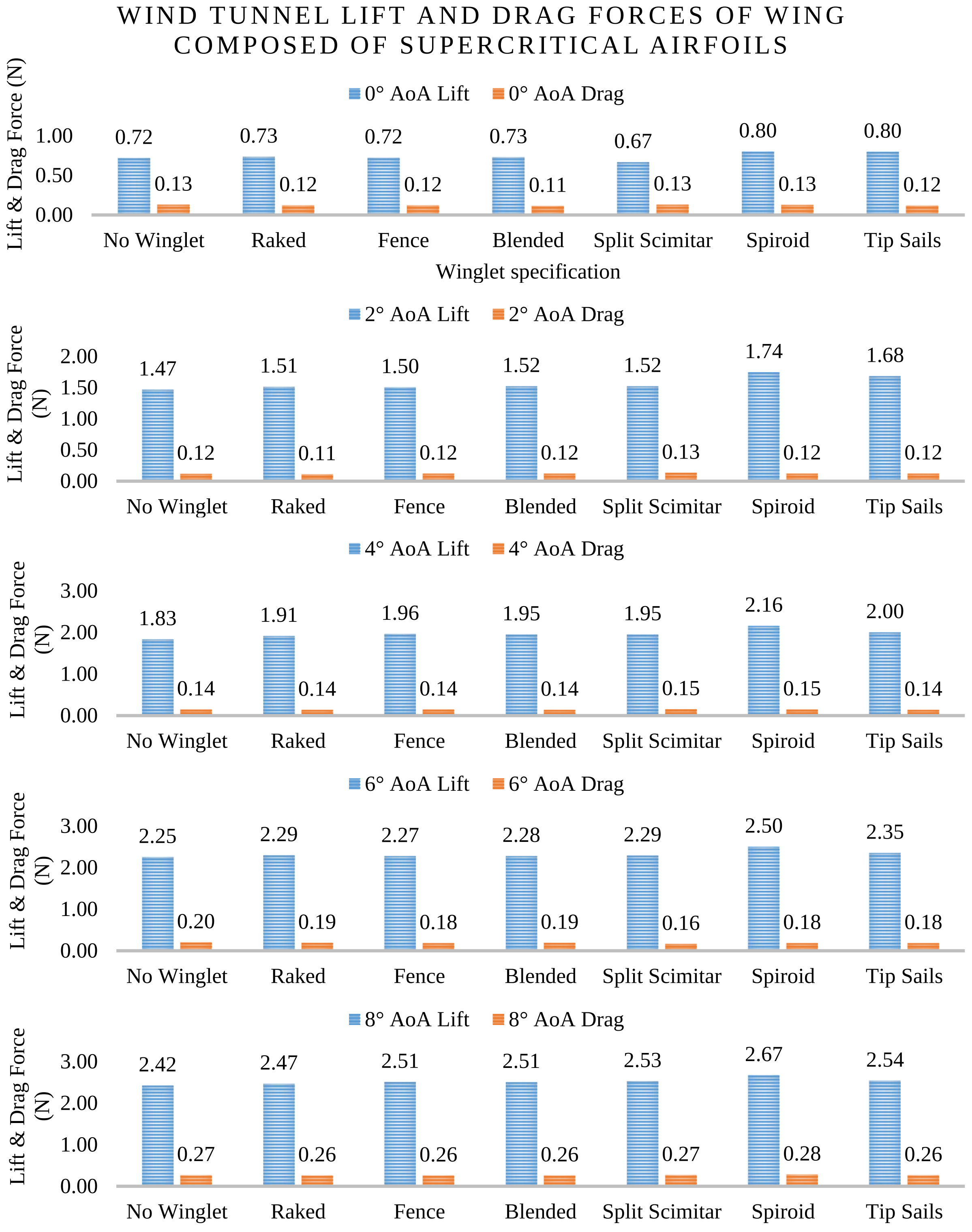

Figure 47. Wind Tunnel Lift and Drag Forces of Wing Composed of Supercritical Airfoils

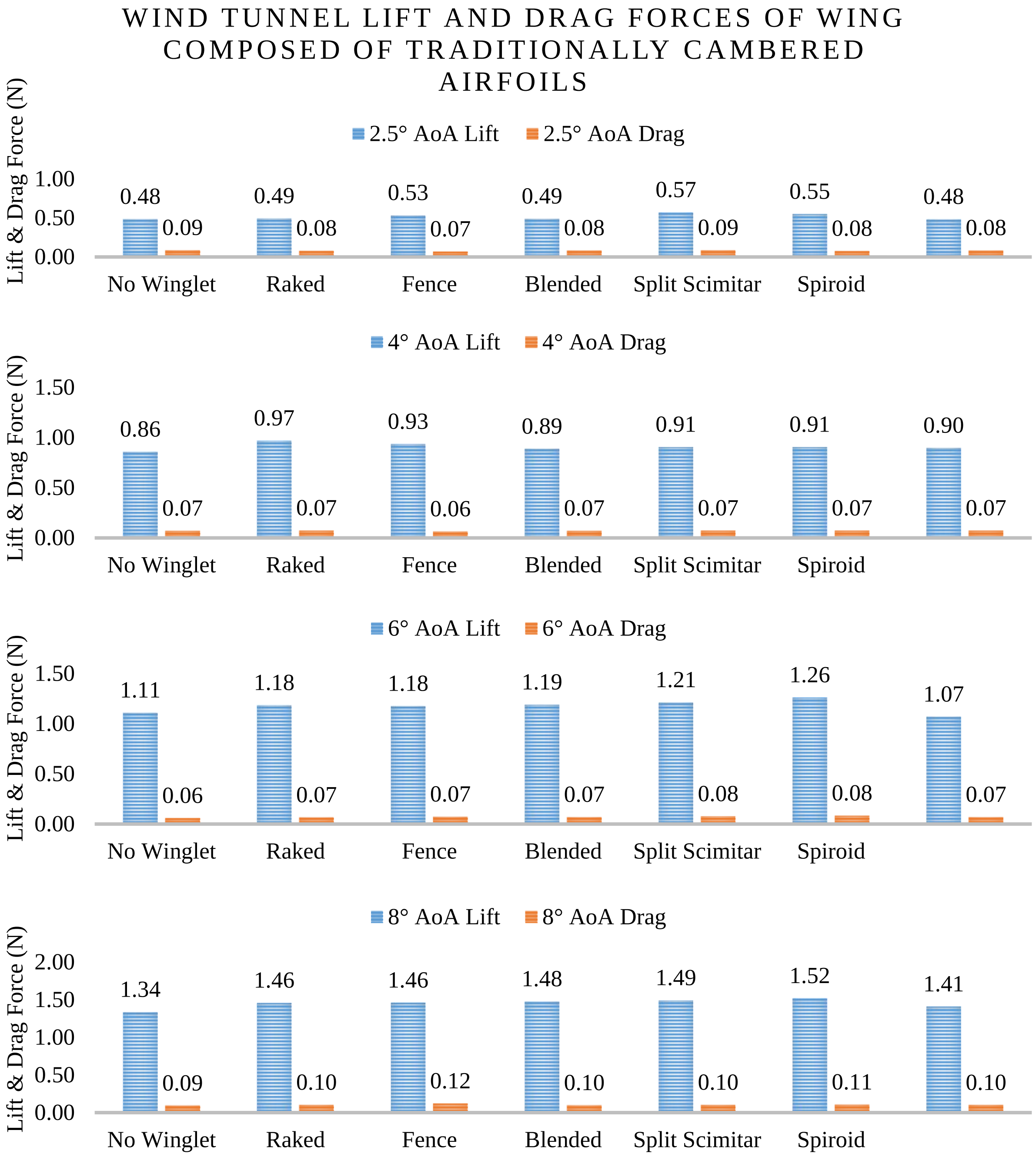

Figure 48. Wind Tunnel Lift and Drag Forces of Wing Composed of Traditionally Cambered Airfoils

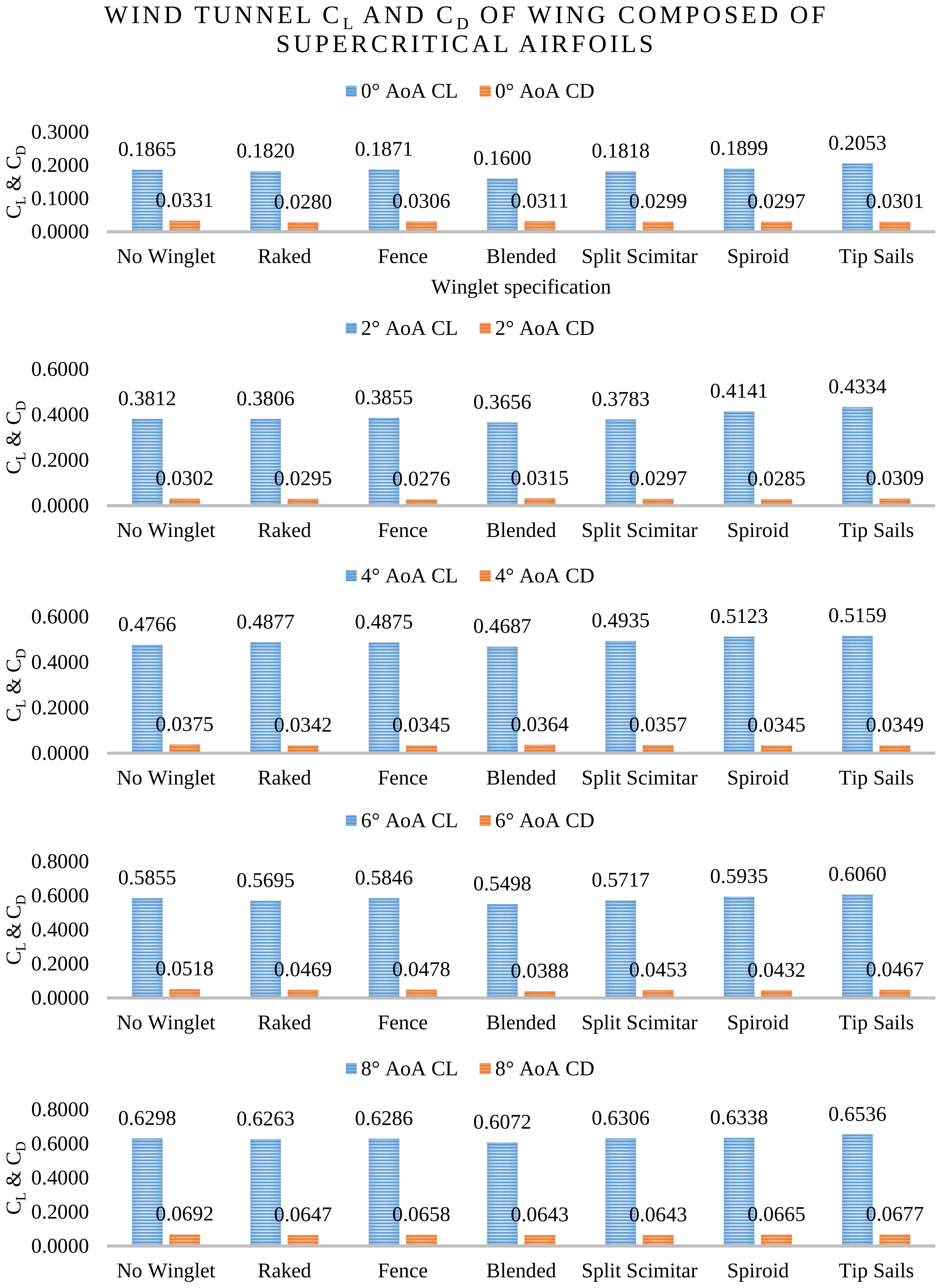

Figure 49. Wind Tunnel C_l & C_d of Wing Composed of Supercritical Airfoils

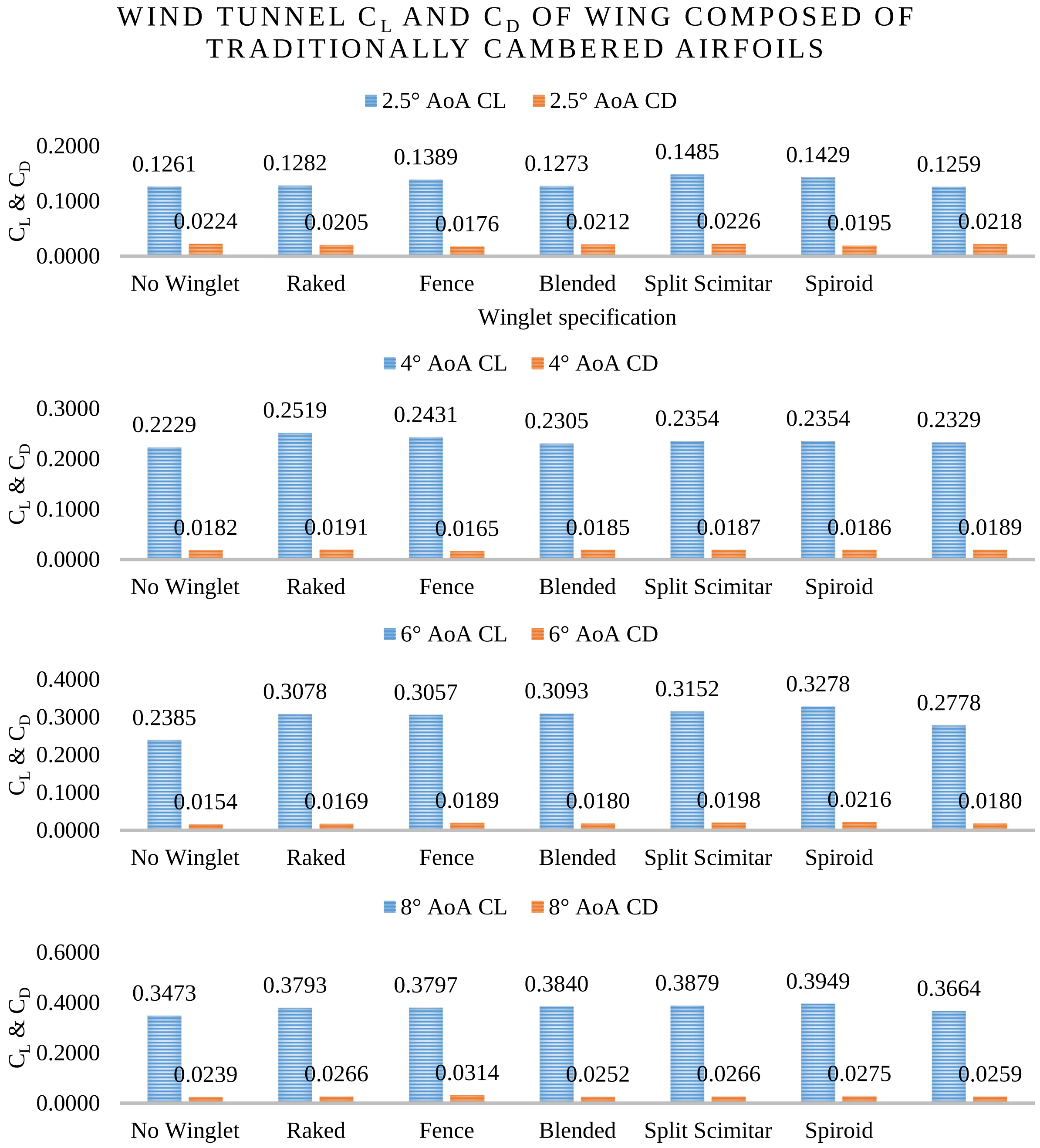

Figure 50. Wind Tunnel C_l & C_d of Wing Composed of Traditionally Cambered Airfoils

Figure 51. Wind Tunnel C_l / C_d of Wing Composed of Supercritical Airfoils

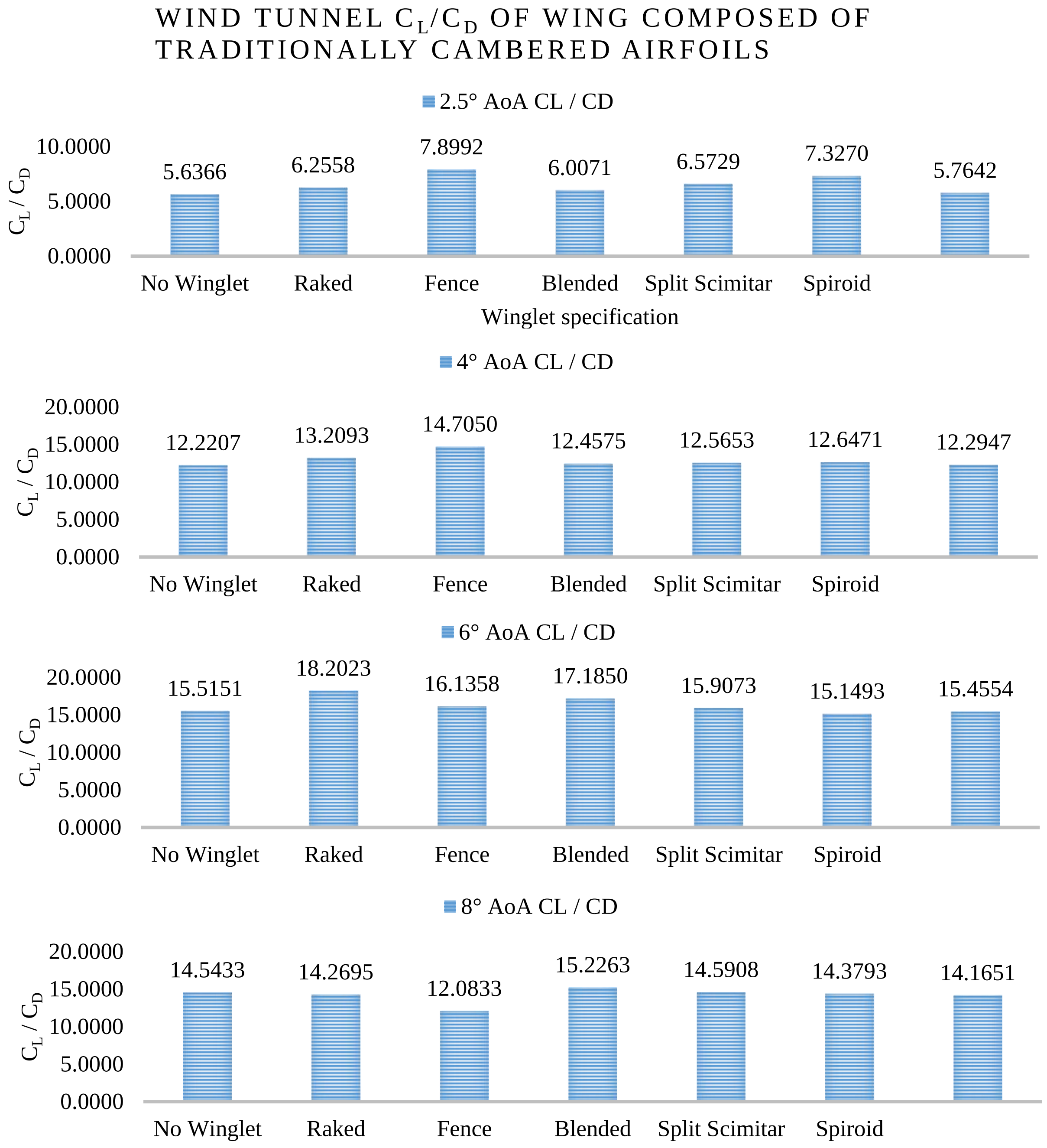

Figure 52. Wind Tunnel C_l / C_d of Wing Composed of Traditionally Cambered Airfoils

4.3 Analysis of Wing Composed of Supercritical Airfoils

Several winglet profiles provided increases in aerodynamic efficiency for both sets of wings, as expected by industry research and practices. However, it must be stated that these are ideal theoretical results and do not represent reported performance statistics of real-time aircraft operation. Impacts of parasitic drag such as skin, form, and interference types are not considered in this study's scope. With this consideration in mind, simulation of the supercritical wing indicates an approximately 21% improvement in C_l / C_d when a spiroid winglet is applied. This is relative to performance at a 2° AoA, which is conducive to cruise conditions of passenger jet aircraft. Compared with the other results gained from the simulation of the supercritical wing, this ranks highest overall. This winglet is a unique design that is still in explorational phases of implementation, having only limited applications to aircraft to date. The vortex structure analysis in CFD-Post indicated that the wing with the spiroid winglet produced vorticity at the furthest extent possible from the main surfaces of the wing, enabling it to generate lift more effectively. The velocity curl magnitude of this rotating flow structure reached 74.9 (s^{-1}), one of the lowest magnitudes out of all the winglets applied to this wing type.

Winglets underperforming this wingtip device are the blended, raked and fence winglets. The blended winglet provided slight improvements to aerodynamic efficiency amounting to approximately 1%. The raked variant maintained an approximate C_l / C_d ratio increase of 10% at cruise conditions over the bare wing. Vortical structure of the raked winglet's turbulence remains along the trailing edge of the winglet but does not form along the main wing's structure due to the increased sweep angle of the winglet's geometry. The fence winglet design implemented in this study proved to be detrimental to wind aerodynamic performance, resulting in a reduction in efficiency of 4.86% at cruise. It is evident that the vorticity produced behind its geometry interferes with lift generation within the last 2 to 3 meters of the wing. The turbulence does not stay confined to the winglet itself, but instead spreads slightly behind the main trailing edge of the wing, reducing performance. This wingtip device was utilized on early Airbus models but was replaced by the 'sharklet' type upon the widespread industry acceptance of the blended-style winglet.

The split scimitar winglet proved to be very effective at the lowest angle of attack on the supercritical wing, providing as much as 18.97% increase over the performance of the bare wing. However, its implementation at higher angles of attack proved to be disadvantageous until significantly higher climb angles are reached, such as 8° as shown by the findings of this study. This wingtip device provides an improvement by creating two separate vortical structures local to the winglet, each being located at the upper and lower tips of the winglet. The magnitude of spread that these vortical structures exhibit appears to be moderate. All these vortices are located further away from the main lift-producing geometry of the wing, causing an increase in the C_l / C_d ratio. However, it is likely that the lowermost vortices contribute significantly to downwash, which in turn decreases the lift of the wing by redirecting the lift force vector slightly rearwards, adding a stronger drag component. The tip sail winglets proved to be very beneficial to the wing's aerodynamic efficiency across the entire range of flight angles, increasing significantly over the others when the aircraft is climbing in altitude. The tip sails are similarly capable in efficiency improvement, producing a comparatively low rate of vortex rotation in several vortical structures which remain along the trailing edges of the wingtip device's structure. While the magnitude of velocity curl of the tip sails may be higher than other underperforming winglet designs, the small surface area contributes to the addition of very little drag force. Table 7 below shows the simulation performance of each winglet on the supercritical wing at all studied angles of attack.

Table 7. Supercritical Wing Simulation Efficiency (C_l / C_d Percent Improvement)

	Blended	Raked Tip	Split Scimitar	Fence Tip	Spiroid	Tip Sails
0°	1.78	14.00	18.97	-5.42	15.30	16.16
2°	1.05	10.12	-14.44	-4.86	20.90	17.86
4°	-3.17	10.28	-18.34	-6.14	22.69	16.61
6°	-5.84	16.90	-21.94	-8.91	31.46	21.06
8°	-12.24	31.06	7.48	-10.97	47.52	34.24

Following this, the analysis of the experimental testing of the supercritical airfoil was performed. It is important to note that due to the atmosphere of the testing chamber, the fluid was more viscous, and its density was much higher as it is near sea level at approximately 20° C. This increased viscosity led to more layer separation at the trailing edge of the airfoil, which led to slight impacts in trends and winglet performances in comparison to the simulation. It is apparent from physical testing that the spiroid winglet is the most suitable choice for cruise conditions (2° AoA) with an efficiency improvement of 15%,. However, this same design choice causes performance to drop when the aircraft is climbing in altitude. The application of tip sails provided the second highest magnitude of aerodynamic efficiency improvement at 11.23%. Following this, the experimental portion shows that the fence wingtip device provides a 0.83% improvement over the bare wing. As can be seen in the vortical structure of the fence winglet, the vorticity tends to spread out from behind the winglet structure itself, impacting lift generation of the main airfoil, as shown in Fig 53.

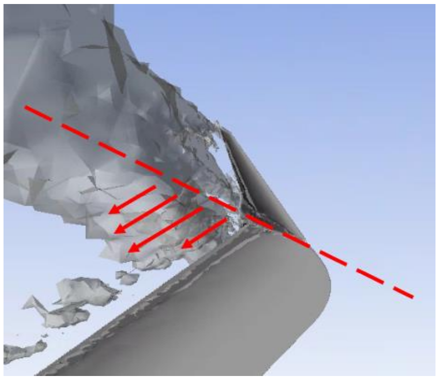

Figure 53. Fence Winglet Turbulence Attachment at 0° AoA

Table 8. Supercritical Wing Wind Tunnel Efficiency (C_l / C_d Percent Improvement)

	Blended	Raked Tip	Split Scimitar	Fence Tip	Spiroid	Tip Sails
0°	15.65	8.69	-8.65	-8.65	13.67	21.09
2°	2.09	10.81	-7.98	0.83	15.06	11.23
4°	12.16	11.28	1.26	8.64	16.70	16.45
6°	7.46	8.34	8.34	11.63	21.60	14.95
8°	6.42	4.94	4.94	7.79	4.72	6.07

One disparity that appeared in the experimental results is the fence and blended winglet's efficiency improvements. This is likely due to the flow's property differences inside the wind tunnel in comparison to those experienced at altitude, leading to different results. For this reason, the simulation's efficiencies for this wing-winglet combination are regarded with higher accuracy. However, the results following this inconsistency line up as expected.

4.4 Analysis of Wing Composed of Traditionally Cambered Airfoils

The performance results of the traditional wing design align closely with industry-reported efficiency improvements for the Boeing 737-800. In a 2009 article published by *AERO* magazine it was reported that when blended winglets developed by Air Partners, Inc. were applied, fuel savings and emissions reduction were recorded at approximately 3.5% and 4% respectively (Freitag and Schulze 2009). This aligns almost identically to the performance of the traditionally cambered wing and blended winglet combination analyzed in this study. At angles of attack respective to cruise conditions, a 5.58% efficiency improvement of C_l / C_d was observed from simulations in ANSYS. The split scimitar winglet also appears to be one of the best choices for this style wing, with one of the highest performances in the simulative portion. In industry application, many aircraft designed with similar airfoils utilize these winglet designs. The spiroid winglet's results are somewhat inconclusive, as they directly contrast each other. This is likely due to differences in flow properties and resulting drag generation. The tip sails provide little to no enhancement to this style wing, with most C_l / C_d readings being lower than that of the bare wing. This is in direct contrast to the supercritical wing, which relies on the efficacy of the tip sails to provide one of the best results in terms of lift and drag. It is shown by the results gathered that blended, raked, split scimitar, and fence-tip winglets all provide increases in aerodynamic efficiency while the exploratory winglets perform poorly.

Table 9. Traditional Wing Simulation Efficiency (C_l / C_d Percent Improvement)

	Blended	Raked Tip	Split Scimitar	Fence Tip	Spiroid	Tip Sails
2.5°	2.29	1.40	2.28	0.24	-0.93	1.11
4°	3.47	1.89	4.82	1.02	-2.39	0.21
6°	5.58	2.35	7.93	1.83	7.57	-2.27
8°	6.29	2.57	9.89	2.10	2.49	-2.90

Table 10. Traditional Wing Wind Tunnel Efficiency (C_l / C_d Percent Improvement)

	Blended	Raked Tip	Split Scimitar	Fence Tip	Spiroid	Tip Sails
2.5°	6.57	10.99	16.61	40.14	29.99	2.26
4°	1.94	8.09	2.82	20.33	3.49	0.61
6°	10.76	17.32	2.53	4.00	-2.36	-0.38
8°	4.70	-1.88	0.33	-16.92	-1.13	-2.60

CHAPTER 5

CONCLUSIONS AND RECOMMENDATIONS

5.1 Notable Findings and Deliverables

It is clear from the study's findings that wings designed with supercritical airfoils benefit from distinctly different varieties of wingtip devices than those used on wings utilizing traditionally cambered airfoils, the wing platform upon which winglets were first based. Portions of this work included simulations as well as experimental testing which was utilized to substantiate the findings from ANSYS Fluent. The lift and drag forces as well as the respective coefficients were determined for each wing-winglet combination at multiple angles of attack, and visualization of vortical structures as well as velocity swirl vectors were generated in CFD-Post.

It was the expectation of the author that slight winglet differences may be present across the board, with the highest discrepancies between the spiroid and tip sail winglets. This expectation was founded on the fact that the other four winglet types (blended, raked, split scimitar, and fence) are very well-known in the aerospace industry with proven longevity on certain aircraft models. It was believed that the magnitude of the spiroid winglet would lead to excess drag production, negating any positive effects, especially on the conventional wing due to its higher aspect ratio. The biomimetic tip sail concept appeared promising, but its ability to compete with larger winglets such as the blended and split scimitar led to some concern with its ability to relocate and reduce the total magnitude of vorticity behind the tips of each wing.

It became apparent through analysis of the study results that the spiroid winglet and tip sails were the most effective at increasing the lift to drag efficiency of the supercritical wing design up to 20% at low angles of attack and 47% at high angles of attack, despite the author's premonitions. Both the simulation and experimental results found that this design performed the best, followed closely by the raked winglet. In contrast, the tip sails and spiroid winglet performed the least effectively on the conventional wing, often producing reductions in efficiency in comparison to the absence of a winglet. The blended and raked winglets on the conventional wing are the most effective, which aligns closely with choices made by airlines utilizing Boeing aircraft. The latest 787 models are offered with a raked winglet, which was the best performing winglet for this application. 737 Models are offered with blended style winglets and split scimitar winglets. It is assumed by the author that the high disparity between efficiency improvements of the supercritical wing versus that of the conventional wing is due to impacts on spanwise flow and its interaction with layer separation produced by each airfoil.

5.2 Future Research Direction

In the future, it may be useful to further substantiate the trends indicated by the simulation and wind tunnel testing by including physical vorticity visualization utilizing either a water tunnel with dye or introducing a fine particulate or fog to the wind tunnel's flow. This experimentation, when recorded by a high-speed camera, can validate the velocity swirl magnitudes, vortical structure, and vorticity spread as shown by simulative data. To further advance this research, simulations and physical experimentation utilizing these winglet designs can be performed with the aircraft's engines and fuselage design included. This will produce form and interference drag that is closer in accuracy to a full-scale aircraft in its entirety. This, in theory, should represent the overall accuracy of these designs when implemented on a fully realized aircraft body. Stress testing can also highlight the best winglets to implement, as this study did not include the structural strength of the wings and winglets within its scope. For example, the spiroid winglet may have produced a highly efficient outcome for the supercritical wing, but also has the most mass and produces the most lift and drag forces overall. These forces may prompt the need for a stronger wing structure near the root; this cost may make the upgrade to a spiroid winglet less desirable over the savings in fuel consumption it can provide over time. Likewise, it may prove worthwhile to determine at what frequencies the tip sail winglet begins to vibrate in high velocity flows, as their thin profiles may prove to be structurally weak with the current materials used for wing construction.

REFERENCES

Al-Atabi, Mushtak. 2006. "Aerodynamics of Wing Tip Sails." *Journal of Engineering Science and Technology* 89-98.

ANSYS. 2009. "Realizable k-ε Model." *ANSYS Fluent 12.0 Theory Guide.* 01 23. Accessed 02 01, 2022. https://www.afs.enea.it/project/neptunius/docs/fluent/html/th/node60.htm.

Aviation Partners, Inc. 2019. "Wow! 10 Billion Gallons of Jet Fuel Saved / 105 Million Tons of Carbon Dioxide Eliminated." *Aviation Partners Boeing.* September 16. Accessed September 29, 2021. http://www.aviationpartnersboeing.com/pdf/pr/2019/API%2010%20Billions%20Gallons%20of%20Jet%20Fuel%20Saved%2016sep19.pdf.

Bahrami, M. 2009. *Introduction and Properties of Fluids.* January. Accessed 04 20, 2022. https://www.sfu.ca/~mbahrami/ENSC%20283/Notes/Intro%20and%20Fluid%20Properties.pdf.

Boeing. 2022. *Boeing Next-Generation 737.* Accessed 04 19, 2022. https://www.boeing.com/commercial/737ng/.

Brady, Chris. n.d. *Boeing 737 Winglets.* Accessed October 4, 2021. http://www.b737.org.uk/winglets.htm#ATWinglets.

Center, NASA John H. Glenn Research. 2021. "Lift to Drag Ratio." *National Aeronautics and Space Administration.* May 13. Accessed 02 22, 2022. https://www.grc.nasa.gov/www/k-12/airplane/ldrat.html.

Clark, Joe, interview by M. J. Smith, N. Komerath, R. Ames, O. Wong and J. Pearson. 1999. *President of Aviation Partners, Inc.* (July 12).

Cosin, R., F. Catalano, L. Correa, and R. Entz. 2010. "Aerodynamic analysis of multi-winglets for low speed aircraft." *27th International Congress of the Aeronautical Sciences.* Nice. 1622-1631. Accessed October 4, 2021.

Freitag, William, and Terry E Schulze. 2009. "Blended Winglets Improve Performance." *AERO,* September: 9-12.

Gudmundsson, Snorri. 2014. *General Aviation Aircraft Design.* Boston: Butterworth-Heinemann.

Guerrero, J. E., M. Sanguineti, and K. Wittkowski. 2020. "Variable cant angle winglets for improvement of aircraft flight performance." *Meccanica* 1917-1947.

Guerrero, J. E., Dario Maestro, and Alessandro Bottaro. 2012. "Biomimetic spiroid winglets for lift and drag control." *Comptes Rendus Mecanique* 67-80.

Güzelbey, Ibrahim Halil, Yüksel Eraslan, and Mehmet Hanifi Doğru. 2018. "Effects of Taper Ration on Aircraft Wing Aerodynamic Parameters: A Cooperative Study." *3rd International Mediterranean Science and Engineering Congress (IMSEC 2018).* Adana. 1-6.

Jones, W P, and B E Launder. 1972. "The prediction of laminarization with a two-equation model of turbulence." *International Journal of Heat and Mass Transfer* 304.

Kermode, Alfred Cotterill, R. H. Barnard, and D. R. Philpott. 2006. *Mechanics of Flight.* Harlow: Pearson Education.

Krishnan, Sivaraj Gopal, Mohammad Hafifi Ishak, Mohammad Azwan Nasirudin, and Farzad Ismail. 2020. "Investigation of Aerodynamic Characteristics of a Wing Model With RGV Winglet." *Journal of Aerospace Technology and Management.*

NASA John H. Glenn Research Center. 2021. *Wing Geometry Definitions.* May 13. Accessed October 2, 2021. https://www.grc.nasa.gov/www/k-12/airplane/geom.html.

National Aeronautics and Space Administration. 2017. *Robert T. Jones.* August 7. Accessed October 3, 2021. https://www.nasa.gov/langley/hall-of-honor/robert-t-jones.

Obert, Ed. 2009. *Aerodynamic Design of Transport Aircraft.* Delft: IOS Press.

OpenFOAM. 2016. "k-epsilon." *OpenFOAM: User Guide v2112.* Accessed 02 01, 2022. https://www.openfoam.com/documentation/guides/latest/doc/guide-turbulence-ras-k-epsilon.html.

Ozturk, Seyda, and Ilker Ors. 2020. "An overview for effects on aerodynamic performance of using winglets and wingtip devices on aircraft." *International Journal of Aeronautics and Astronautics* 1-11.

Petrescu, Relly Victoria Virgil, Raffaella Aversa, Bilal Akash, Juan M. Corchado, Antonio Apicella, and Florian Ion Tiberiu Petrescu. 2017. "Home at Airbus." *Journal of Aircraft and Spacecraft Technology* 97-118.

Roskam, Jan. 1979. *Airplane Flight Dynamics and Automatic Flight Controls.* Ottawa, Kansas: Roskam Engineering and Aviation Corporation. Accessed October 3, 2021.

Sforza, Pasquale. 2014. "Commercial Airplane Design Principles." 119-212. Butterworth-Heinemann.

Shih, C., L. Lourenco, L. Van Dommelen, and A. Krothapalli. 1992. "Unsteady flow past an airfoil pitching at a constant rate." *American Institute of Aeronautics and Astronautics* 1153-1161.

The National Aeronautics and Space Administration. 2008. *NASA Dryden Technology Facts - The Supercritical Airfoil.* March 3. Accessed September 30, 2021. https://www.nasa.gov/centers/dryden/about/Organizations/Technology/Facts/TF-2004-13-DFRC.html.

Tucker, Vance A. 1993. "Gliding Birds: Reduction of Induced Drag By Wing Tip Slots Between The Primary Feathers." *Journal of Experimental Biology* 285-310.

Vincenti, Walter G. 2005. "Robert Thomas Jones 1910 - 1999." *Biographical Memoirs.* Washington, D.C.: The National Academies Press.

Winslow, Justin, Hiraku Otsuka, Bharath Govindarajan, and Inderjit Chopra. 2018. "Basic Understanding of Airfoil Characteristics at Low Reynolds Numbers." *Journal of Aircraft* 1050-1061.

APPENDIX A

DESIGN PARAMETERS

Table 11. Wing Geometrical Reference Values

		No winglet	Blended	Raked	Split scimitar	Fence	Spiroid	Tip sails
Wing Composed of Supercritical Airfoils	Planform area (m^2)	44.465	46.43	45.35	47.785	45.645	48.785	44.79
	Wingspan (m)	15	15.48	15.90	16.01	15.68	17.29	15.66
Wing Composed of Asymmetric Airfoils	Planform area (m^2)	52.625	54.73	53.705	56.995	54.42	57.635	53.125
	Wingspan (m)	15	15.48	15.99	16.22	16.01	17.32	15.79

Table 12. Linear Mesh Sizing Metrics

Geometry	Specification
Primary domain	~3500 mm
Intermediate domain (body of influence method)	250 mm
Wing upper / lower surfaces (face sizing)	250 mm
Leading edge (edge sizing)	25 mm
Trailing edge (edge sizing)	5 mm
Sharp intersections (edge sizing)	1 mm

Table 13. Simulation Inlet Conditions (at 11.5 km Altitude)

	Measure
Temperature	217.79 K (approx. -55.36°C)
Density	0.3414 kg/m^3
Dynamic viscosity	1.428e^{-5} kg/m-s
Velocity	230 m/s
Reynolds Number (Supercritical / Conventional)	$24.9\text{x}10^6$ / $21.8\text{x}10^6$

Table 14. Experimental Flow Conditions (at Sea Level)

	Measure
Temperature	293.15 K (approx. 20°C)
Density	1.225 kg/m^3
Dynamic viscosity	$1.825\text{x}10^{-5}$ kg/m-s
Velocity	12 m/s
Reynolds Number (Supercritical / Conventional)	$1.05\text{x}10^5$ / $9.17\text{x}10^4$

Figure 54. Contoured Wing Mount

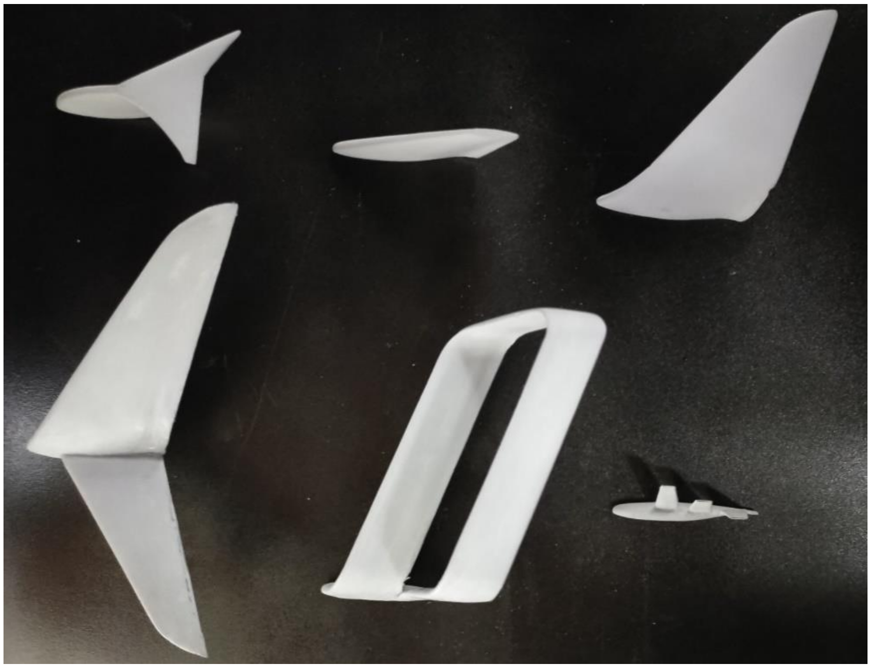

Figure 55. 3D Printed Winglets

Principle

- Equal linear scaling of dimensions in all coordinate directions
- All angles and flow directions are preserved

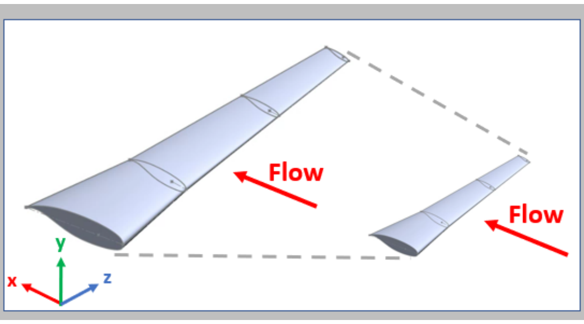

Application

- Scaling factor of ~ 1/35 (15 m → 17 inches) in X,Y,Z directions
- The same flow vectors and angles of attack are designated as they are in ANSYS

Figure 56. Geometric Similarity Criteria Analysis

Principle

- Length scale (geometrical similarity!) matches the time scale ratio
- Froude (*Fr*) number

	Supercritical		Traditional	
Variable	Prototype (*p*)	Model (*m*)	Prototype	Model
MAC *(m)*	4.521	0.1301	3.957	0.1139
V *(velocity, m/s)*	230	12	230	12
ρ *(density, kg/m3)*	0.3414	1.225	0.3414	1.225
μ *(dynamic viscosity, kg/m-s)*	1.43E-05	1.83E-05	1.43E-05	1.83E-05
F *(lift force, N)*	176044	0.509	123268	0.539

$$FR_p = \frac{V_p^2}{g*L_p} = \frac{V_m^2}{g*L_m} = FR$$

Application

$$FR_p = \frac{V_p^2}{9.77*MAC_p} = \frac{V_m^2}{9.81*MAC_m}$$

$FR_{Supercritical}$ 1197.64 ≠ 112.83
...to match, $V_m = 39.09$ m/s

$FR_{Traditional}$ 1368.34 ≠ 128.87
...to match, $V_m = 39.10$ m/s

Figure 57. Kinematic Similarity Criteria Analysis

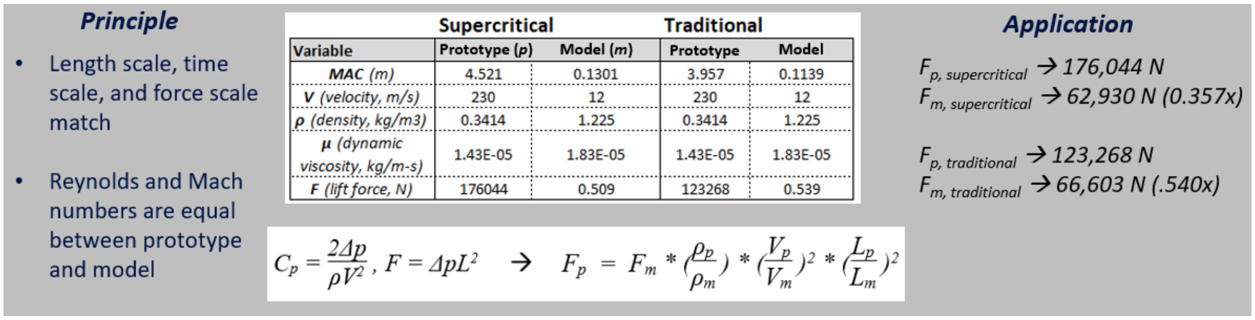

Principle

- Length scale, time scale, and force scale match
- Reynolds and Mach numbers are equal between prototype and model

	Supercritical		Traditional	
Variable	Prototype (*p*)	Model (*m*)	Prototype	Model
MAC *(m)*	4.521	0.1301	3.957	0.1139
V *(velocity, m/s)*	230	12	230	12
ρ *(density, kg/m3)*	0.3414	1.225	0.3414	1.225
μ *(dynamic viscosity, kg/m-s)*	1.43E-05	1.83E-05	1.43E-05	1.83E-05
F *(lift force, N)*	176044	0.509	123268	0.539

$$C_p = \frac{2\Delta p}{\rho V^2},\ F = \Delta p L^2 \quad \rightarrow \quad F_p = F_m * (\frac{\rho_p}{\rho_m}) * (\frac{V_p}{V_m})^2 * (\frac{L_p}{L_m})^2$$

Application

$F_{p,\ supercritical}$ → *176,044 N*
$F_{m,\ supercritical}$ → *62,930 N (0.357x)*

$F_{p,\ traditional}$ → *123,268 N*
$F_{m,\ traditional}$ → *66,603 N (.540x)*

Figure 58. Dynamic Similarity Criteria Analysis

APPENDIX B

STUDY RESULTS

Table 15. Simulation Lift and Drag Forces and Coefficients of Wing Composed of Supercritical Airfoils

0° AoA	No Winglet	Blended	Raked Tip	Split Scimitar	Fence Tip	Spiroid	Tip Sails
Lift Force	188392	194224	192639	196454	190455	200787	189191
Drag Force	9274	9892	8756	8557	10435	9028	8440
Lift Coefficient	0.3966	0.3914	0.3759	0.3833	0.3874	0.4558	0.3938
Drag Coefficient	0.0195	0.0199	0.0171	0.0167	0.0212	0.0205	0.0176
Cl/Cd	20.3171	19.6362	21.9941	22.9533	18.2473	22.2445	22.4104
COPx	-2.8680	-3.1364	-2.9617	-3.3162	-3.0427	-3.3735	-2.9459
COPy	0.6798	0.7459	0.7037	0.7971	0.7129	0.8600	0.7098
COPz	-5.5363	-6.0997	-5.7827	-6.4408	-5.8959	-6.6128	-5.6943

2° AoA	No Winglet	Blended	Raked Tip	Split Scimitar	Fence Tip	Spiroid	Tip Sails
Lift Force	257954	268171	272007	259475	265137	286084	268937
Drag Force	12295	13131	12226	15006	13536	11710	11292
Lift Coefficient	0.5430	0.5404	0.5308	0.5063	0.5393	0.6494	0.5597
Drag Coefficient	0.0259	0.0265	0.0239	0.0293	0.0275	0.0266	0.0235
Cl/Cd	20.9826	20.4214	22.2537	17.2913	19.5892	24.4323	23.8179

4° AoA	No Winglet	Blended	Raked Tip	Split Scimitar	Fence Tip	Spiroid	Tip Sails
Lift Force	322724	330888	346453	315228	328372	369207	345754
Drag Force	16532	17507	16091	19774	17921	15418	15186
Lift Coefficient	0.6794	0.6667	0.6760	0.6151	0.6679	0.8381	0.7196
Drag Coefficient	0.0348	0.0353	0.0314	0.0386	0.0365	0.0350	0.0316
Cl/Cd	19.5224	18.9033	21.5290	15.9430	18.3240	23.9526	22.7646

6° AoA	No Winglet	Blended	Raked Tip	Split Scimitar	Fence Tip	Spiroid	Tip Sails
Lift Force	371527	374981	414862	364158	374268	450167	418207
Drag Force	21831	23394	20852	27418	24142	20123	20299
Lift Coefficient	0.7821	0.7554	0.8095	0.7106	0.7613	1.0219	0.8704
Drag Coefficient	0.0460	0.0471	0.0407	0.0535	0.0491	0.0457	0.0423
Cl/Cd	17.0174	16.0244	19.8941	13.2838	15.5013	22.3704	20.6007

8° AoA	No Winglet	Blended	Raked Tip	Split Scimitar	Fence Tip	Spiroid	Tip Sails
Lift Force	404079	404564	471185	469964	424383	526633	491377
Drag Force	29805	34001	26519	32252	35158	26330	26997
Lift Coefficient	0.8507	0.8152	0.9194	0.9170	0.8632	1.1955	1.0227
Drag Coefficient	0.0627	0.0685	0.0517	0.0629	0.0715	0.0598	0.0562
Cl/Cd	13.5583	11.8986	17.7694	14.5719	12.0710	20.0010	18.2000

Table 16. Simulation Lift and Drag Forces and Coefficients of Wing Composed of Traditionally Cambered Airfoils

	2.5° AoA						
	No Winglet	**Blended**	**Raked Tip**	**Split Scimitar**	**Fence Tip**	**Spiroid**	**Tip Sails**
Lift Force	123268.09	127966	126588	130540	126145	133128	123548
Drag Force	5411	5546	5531	5656	5579	5956	5415
Lift Coefficient	0.3037	0.3058	0.3091	0.3028	0.3056	0.3022	0.3055
Drag Coefficient	0.0135	0.0133	0.0135	0.0131	0.0135	0.0135	0.0134
Cl/Cd	22.5654	23.0815	22.8808	23.0808	22.6195	22.3550	22.8155
	4° AoA						
	No Winglet	**Blended**	**Raked Tip**	**Split Scimitar**	**Fence Tip**	**Spiroid**	**Tip Sails**
Lift Force	171049	178690	176904	182247	176374	184911	173135
Drag Force	6719	6785	6817	6829	6858	7439	6787
Lift Coefficient	0.4255	0.4271	0.4320	0.4228	0.4273	0.4198	0.4282
Drag Coefficient	0.0167	0.0162	0.0167	0.0158	0.0166	0.0169	0.0168
Cl/Cd	25.4632	26.3479	25.9453	26.6907	25.7237	24.8555	25.5173
	6° AoA						
	No Winglet	**Blended**	**Raked Tip**	**Split Scimitar**	**Fence Tip**	**Spiroid**	**Tip Sails**
Lift Force	233975	243364	240662	248167	240402	254536	234802
Drag Force	9246	9105	9288	9081	9323	9347	9491
Lift Coefficient	0.5820	0.5816	0.5877	0.5757	0.5824	0.5779	0.5807
Drag Coefficient	0.0230	0.0218	0.0227	0.0211	0.0226	0.0212	0.0235
Cl/Cd	25.3162	26.7293	25.9118	27.3237	25.7804	27.2328	24.7414
	8° AoA						
	No Winglet	**Blended**	**Raked Tip**	**Split Scimitar**	**Fence Tip**	**Spiroid**	**Tip Sails**
Lift Force	289421	300446	299116	306486	298196	303287	290880
Drag Force	12584	12290	12679	12127	12697	13286	13023
Lift Coefficient	0.7199	0.7181	0.7304	0.7110	0.7224	0.7416	0.7194
Drag Coefficient	0.0313	0.0294	0.0310	0.0281	0.0308	0.0315	0.0322
Cl/Cd	23.0013	24.4488	23.5924	25.2755	23.4847	23.5737	22.3337

Table 17. Velocity Curl Magnitudes (s^{-1}) of Wing Composed of Supercritical Airfoils

Winglet Configuration	Velocity Curl Magnitude (s^{-1})
No winglet	428.7
Blended	162.2
Raked	409.4
Split Scimitar	68.5
Fence	132.3
Spiroid	74.9
Tip Sails	165.1

Table 18. Velocity Curl Magnitudes (s^{-1}) of Wing Composed of Traditionally Cambered Airfoils

Winglet Configuration	Velocity Curl Magnitude (s^{-1})
No winglet	635.3
Blended	318.6
Raked	578.3
Split Scimitar	251.0
Fence	102.3
Spiroid	105.2
Tip Sails	565.8